

Dominantly acting variants in ARF3 have disruptive consequences on Golgi integrity and cause microcephaly recapitulated in zebrafish

Giulia Fasano

Ospedale Pediatrico Bambino Gesù

Valentina Muto

Ospedale Pediatrico Bambino Gesù

Francesca Clementina Radio

Genetic and Rare Disease Research Division, Bambino Gesù Children's Hospital IRCCS, Rome, Italy

<https://orcid.org/0000-0003-1993-8018>

Martina Venditti

Ospedale Pediatrico Bambino Gesù

Alban Ziegler

Département de Génétique, CHU d'Angers

Giovanni Chillemi

Tuscia University <https://orcid.org/0000-0003-3901-6926>

Annalisa Vetro

Pediatric Neurology, Neurogenetics and Neurobiology Unit and Laboratories, Meyer Children's Hospital, University of Florence

Francesca Pantaleoni

<https://orcid.org/0000-0003-0765-9281>

Simone Pizzi

Bambino Gesù Children's Hospital

Libenzio Conti

Ospedale Pediatrico Bambino Gesù, IRCCS, 00146 Rome <https://orcid.org/0000-0001-9466-5473>

Stefania Petrini

Bambino Gesù Children's Hospital

Simona Coppola

Istituto Superiore di Sanità

Alessandro Bruselles

Istituto Superiore di Sanità <https://orcid.org/0000-0002-1556-4998>

Ingrid Guarnetti Prandi

University of Pisa, 56124 Pisa, Italy

Balasubramanian Chandramouli

Super Computing Applications and Innovation, CINECA

Magalie Barth

Céline Bris

Département de Génétique, CHU d'Angers

Donatella Milani

Fondazione IRCCS Ca' Granda Ospedale Maggiore Policlinico

Angelo Selicorni

ASST Lariana

Marina Macchiaiolo

Ospedale Pediatrico Bambino Gesù, IRCCS

Michaela Gonfiantini

Ospedale Pediatrico Bambino Gesù, IRCCS

Andrea Bartuli

Bambino Gesù Children's Hospital

Renzo Guerrini

Children's Hospital A. Meyer-University of Florence

Anne Slavotinek

University of California and San Francisco

Maria Iascone

ASST Papa Giovanni XXIII

Bruno Dallapiccola

Bambino Gesù Children Hospital

Antonella Lauri (✉ antonella.lauri@opbg.net)

Ospedale Pediatrico Bambino Gesù, IRCCS

Marco Tartaglia

Ospedale Pediatrico Bambino Gesù <https://orcid.org/0000-0001-7736-9672>

Article

Keywords: ARF3, Golgi integrity, zebrafish, de novo missense variants

Posted Date: August 10th, 2021

DOI: <https://doi.org/10.21203/rs.3.rs-678090/v1>

License:  This work is licensed under a Creative Commons Attribution 4.0 International License.

[Read Full License](#)

Additional Declarations: There is **NO** Competing Interest.

Version of Record: A version of this preprint was published at Nature Communications on November 11th, 2022. See the published version at <https://doi.org/10.1038/s41467-022-34354-x>.

1 **Dominantly acting variants in ARF3 have disruptive consequences on Golgi
2 integrity and cause microcephaly recapitulated in zebrafish**

3

4 Giulia Fasano^{1,16}, Valentina Muto^{1,16}, Francesca Clementina Radio^{1,16}, Martina
5 Venditti¹, Alban Ziegler^{2,3}, Giovanni Chillemi^{4,5}, Annalisa Vetro⁶, Francesca
6 Pantaleoni¹, Simone Pizzi¹, Libenzio Adrian Conti⁷, Stefania Petrini⁷, Simona
7 Coppola⁸, Alessandro Bruselles⁹, Ingrid Guarnetti Prandi¹⁰, Balasubramanian
8 Chandramouli¹¹, Magalie Barth^{2,3}, Céline Bris^{2,3}, Donatella Milani¹², Angelo Selicorni¹³,
9 Marina Macchiaiolo¹, Michaela V Gonfiantini¹, Andrea Bartuli¹, Renzo Guerrini⁶, Anne
10 Slavotinek¹⁴, Maria Iascone¹⁵, Bruno Dallapiccola¹, Antonella Lauri^{1,17*}, Marco
11 Tartaglia^{1,17*}

12

13 **Author information**

14 ¹Genetics and Rare Diseases Research Division, Ospedale Pediatrico Bambino Gesù, IRCCS,
15 00146 Rome, Italy.

16 ²Département de Génétique, CHU d'Angers, 49000 Angers, France.

17 ³UFR Santé de l'Université d'Angers, INSERM U1083, CNRS UMR6015, MITOVASC, SFR
18 ICAT, F-49000 Angers, France.

19 ⁴Institute of Biomembranes, Bioenergetics and Molecular Biotechnologies, Centro Nazionale
20 delle Ricerche, 70126, Bari, Italy.

21 ⁵Department for Innovation in Biological Agro-food and Forest systems (DIBAF), University of
22 Tuscia, 01100 Viterbo, Italy.

23 ⁶Pediatric Neurology, Neurogenetics and Neurobiology Unit and Laboratories, Meyer
24 Children's Hospital, University of Florence, 50139 Florence, Italy

Dominantly acting variants in ARF3 have disruptive consequences on Golgi integrity and cause microcephaly recapitulated in zebrafish
Fasano, Muto, Radio, et al.

25 ⁷Confocal Microscopy Core Facility, Ospedale Pediatrico Bambino Gesù, IRCCS, 00146
26 Rome, Italy.
27 ⁸Centro Nazionale Malattie Rare, Istituto Superiore di Sanità, 00161 Rome, Italy.
28 ⁹Department of Oncology and Molecular Medicine, Istituto Superiore di Sanità, 00161 Rome,
29 Italy.
30 ¹⁰Department of Chemistry and Industrial Chemistry, University of Pisa, 56124 Pisa, Italy
31 ¹¹Super Computing Applications and Innovation, CINECA, 40033 Casalecchio di Reno, Italy.
32 ¹²Pediatric Highly Intensive Care Unit, Fondazione IRCCS Ca' Granda Ospedale Maggiore
33 Policlinico, 20122 Milan, Italy.
34 ¹³Mariani Center for Fragile Children Pediatric Unit, Azienda Socio Sanitaria Territoriale
35 Lariana, 22100 Como, Italy.
36 ¹⁴Department of Pediatrics, Division of Medical Genetics, University of California, San
37 Francisco, San Francisco, CA 94143, USA.
38 ¹⁵Medical Genetics, ASST Papa Giovanni XXIII, 24127 Bergamo, Italy.
39 ¹⁶These authors contributed equally to this work
40 ¹⁷These authors contributed equally to this work
41

42 *Corresponding authors:
43
44 Antonella Lauri
45 Genetics and Rare Diseases Research Division
46 Ospedale Pediatrico Bambino Gesù
47 Viale di San Paolo, 15
48 00146 Rome, Italy
49 Email: antonella.lauri@opbg.net
50
51 Marco Tartaglia
52 Genetics and Rare Diseases Research Division
53 Ospedale Pediatrico Bambino Gesù
54 Viale di San Paolo, 15
55 00146 Rome, Italy
56 Email: marco.tartaglia@opbg.net

57 **Email Addresses**

58
59 Giulia Fasano giulia.fasano@opbg.net
60 Valentina Muto valentina.muto@opbg.net
61 Francesca Clementina Radio fclmentina.radio@opbg.net
62 Martina Venditti martina.venditti@opbg.net
63 Alban Ziegler alban.ziegler@chu-angers.fr
64 Giovanni Chillemi gchillemi@unitus.it
65 Annalisa Vetro annalisa.vetro@meyer.it
66 Francesca Pantaleoni francesca.pantaleoni@opbg.net
67 Simone Pizzi simone.pizzi@opbg.net
68 Adrian Libenzio Conti libenzioadrian.conti@opbg.net
69 Stefania Petrini stefania.petrini@opbg.net
70 Simona Coppola simona.coppola@iss.it
71 Alessandro Bruselles alessandro.bruselles@iss.it
72 Ingrid Guarnetti Prandi ingrid.prandi@gmail.com
73 Balasubramanian Chandramouli b.chandramouli@cineca.it
74 Magalie Barth mabarth@chu-angers.fr
75 Céline Bris cebris@chu-angers.fr
76 Donatella Milani donatella.milani@policlinico.mi.it
77 Angelo Selicorni angelo.selicorni61@gmail.com
78 Marina Macchiaiolo marina.macchiaiolo@opbg.net
79 Michaela Veronika Gonfiantini. mveronik.gonfiantini@opbg.net
80 Andrea Bartuli andrea.bartuli@opbg.net
81 Renzo Guerrini renzo.guerrini@meyer.it
82 Anne Slavotinek anne.slavotinek@ucsf.edu
83 Maria Iascone miascone@asst-pq23.it
84 Bruno Dallapiccola bruno.dallapiccola@opbg.net
85 Antonella Lauri antonella.lauri@opbg.net
86 Marco Tartaglia marco.tartaglia@opbg.net

87 **Abstract**

88 Vesicle biogenesis, trafficking and signaling via the ER-Golgi network support essential
89 processes during development and their disruption can lead to neurodevelopmental
90 disorders and neurodegeneration. We report that *de novo* missense variants in *ARF3*,
91 encoding a small GTPase regulating Golgi structure and function, cause a
92 neurodevelopmental disease showing microcephaly and progressive cortical atrophy,
93 with microsomia and rib anomalies in severely affected subjects, suggesting a
94 pleiotropic effect. All microcephaly-associated variants clustered in the guanine
95 nucleotide binding pocket and perturbed the biochemical behavior of the protein by
96 stabilizing it in a GTP-bound state. Functional analysis proved the disruptive
97 consequences of the variants on Golgi integrity, and brain and body plan formation. In-
98 depth analysis in zebrafish embryos expressing *ARF3* mutants traced back the
99 developmental alterations to defective gastrulation cell movements as the earliest
100 detectable effect. Our findings document a role of *ARF3* in Golgi homeostasis and
101 demonstrate an obligate dependence for early development.

102 **Introduction**

103 The Golgi apparatus (GA) is a polarized, membrane network-built organelle
104 responsible for transporting, modifying, and packaging proteins and lipids into vesicles
105 for their delivery to targeted destinations^{1,2}. It is organized as a series of flattened,
106 stacked pouches (known as *cisternae*) that are held together by matrix proteins and
107 microtubules, and are structured into two major networks, the *cis* and *trans*-Golgi
108 compartments, coordinating proper sorting of proteins and lipids received from the
109 endoplasmic reticulum and directing their transport toward the cell membrane^{3,4}. GA
110 organization is highly dynamic and undergoes rapid remodeling in response to different
111 physiological and pathological stimuli *via* various tightly regulated processes involving
112 ribbon disassembly and tubulovesicular conversion as well as repositioning of Golgi
113 stacks⁵. Besides the role of GA in posttranslational modification and sorting of proteins,
114 a large body of studies recently revealed that GA membranes also provide signaling
115 platforms for the regulation of a wide range of cellular processes (e.g., cell polarization,
116 directed migration, stress response, mitosis, and autophagy) orchestrating animal
117 development, suggesting that GA can act as a cell sensor and regulator similarly to
118 other intracellular organelles⁴. Not surprisingly, in the last years, a number of
119 Mendelian disorders have been causally related to the defective or aberrant function
120 of component of the GA-related transport machinery and disrupted GA function and
121 organization, most of which sharing altered neurodevelopment and early-onset
122 neurodegeneration^{6–8}. In these disorders, which have collectively been termed as
123 “Golgopathies”, recurrent features include microcephaly, central nervous system (CNS)
124 defects (e.g., delayed myelination, cortical atrophy, abnormal corpus callosum, and
125 pontocerebellar hypoplasia) and developmental delay (DD)/intellectual disability
126 (ID)^{8,9}.

127 The five members of the ADP-ribosylation factors (ARF) family of small GTPases
128 (ARF1, ARF3-6) regulate key events in vesicular biogenesis, transport and various GA
129 functions, and participate in the control of bidirectional membrane trafficking required
130 for secretion, endocytosis and recycling^{10–13}. These proteins bind to guanine
131 nucleotides with high affinity and specificity, and have a slow intrinsic competence to
132 hydrolyze GTP to GDP^{12,14}. ARF proteins are characterized by a unique myristoylated
133 N-terminal region, a GTP/GDP-interacting pocket, and two domains mediating binding
134 with regulators and effectors (*i.e.*, switch 1 [SW1] and switch 2 [SW2] regions) that
135 undergo a GTP/GDP-dependent structural rearrangement, allowing the GTPase to
136 interact with effectors in its GTP-bound state^{15–17}. Similarly to other members of the
137 RAS superfamily, release of GDP is stimulated by specific guanine nucleotide
138 exchange factors (ARFGEFs), which indirectly favor binding to GTP^{12,18,19}. As a
139 consequence of the conformational change promoted by GTP, the N-terminal
140 myristoylated region is exposed, allowing anchoring of the GTPase to the cytoplasmic
141 leaflet of membranes of different organelles, including *cis* and *trans*-Golgi, plasma
142 membrane (PM) and endosomes, where these proteins exert their function^{12,14,17,20,21}.
143 The intrinsic slow GTPase activity of ARFs is substantially accelerated by specific
144 GTPase-activating proteins (ARFGAPs), which result in protein inactivation and
145 release from membranes^{12,21–23}.

146 To exert their function, ARF proteins interact with a number of effectors, most of which
147 are coat proteins and adaptors^{1,12}; they can also recruit non-coat GA-specific proteins
148 to membranes (*e.g.*, golgin-160 and GCC88)²⁴, which are important for GA structure
149 homeostasis^{25,26}. Evidence shows that ARF proteins actually contribute to the control
150 of GA and organelles structural organization and function^{13,27,28}, and GA dynamics

151 during cell division and cytokinesis in precursor cells^{29–31}. By controlling GA structure,
152 function, cargo sorting and ER-GA targeted trafficking, ARFs actively participate to the
153 fine regulation of key events during embryogenesis (*i.e.*, cell polarity establishment and
154 migration in early gastrulation, neuronal maturation and tissue morphogenesis)³².
155 Indeed, hyperactive *arf1* function in zebrafish results in shortening of the anterior-
156 posterior (AP) axis, a likely consequence of an altered planar cell polarity (PCP)-
157 dependent cell movements, which was also shown in a fly wing morphogenesis
158 model³³. Nevertheless, the underlying mechanisms by which the activity of several
159 ARF proteins on GA organization and trafficking contributes to developmental
160 processes are yet not fully understood.

161 Notwithstanding the pivotal roles of ARF proteins in development, mutations in *ARF*
162 genes have only recently been linked to human disease, with activating missense
163 variants of *ARF1* (MIM: 103180) causing a rare dominant neurodevelopmental disorder
164 (NDD) resulting from defective neuronal migration (MIM: 618185)³⁴. Here, we report
165 *de novo* missense variants in *ARF3* underlying a disorder affecting neurodevelopment
166 and causing neurodegeneration in five patients. *In silico* and *in vitro* analyses
167 strengthened by *in vivo* morphometric and live cell behavioral analyses in fish embryos
168 expressing *ARF3* mutants provide evidence of a variable impact of mutations on
169 protein function and disruptive consequences on GA integrity, brain and body axes
170 development and PCP-dependent gastrulation processes. These findings demonstrate
171 the relevance of *ARF3* function on organelle homeostasis and development.

172 **Results**

173 **ARF3 mutations cause a developmental disorder characterized by microcephaly
174 and cortical atrophy**

175 In the frame of a research program dedicated to subjects affected by unclassified
176 diseases, trio-based exome sequencing allowed us to identify a previously unreported
177 *de novo* ARF3 variant, c.379A>G (p.Lys127Glu; NM_001659.2), as the putative
178 disease-causing event in a girl (Subject 1) with severe syndromic NDD characterized
179 by growth restriction, microcephaly, progressive diffuse cortical atrophy and other brain
180 anomalies at MRI (*i.e.*, lateral ventricular enlargement, progressive pontocerebellar
181 hypoplasia with major involvement of the cerebellar vermis and hypoplasia of corpus
182 callosum), seizures, inguinal hernia, congenital heart defects (CHD) and skeletal
183 involvement (*i.e.*, 11 rib pairs and scoliosis) ([Table 1](#), [Supplementary Figure 1](#),
184 [Supplementary clinical reports](#)). WES data analysis excluded presence of other
185 relevant variants compatible with known Mendelian disorders based on their expected
186 inheritance model and associated clinical presentation, and high-resolution SNP array
187 analysis excluded occurrence of genomic rearrangements. The missense change,
188 which had not previously been reported in population databases, affected an
189 invariantly conserved residue among orthologs, paralogs and other structurally related
190 GTPases of the RAS family ([Supplementary Figure 2a](#)).

191 Through networking and GeneMatcher³⁵, we identified four additional subjects with *de*
192 *novo* ARF3 missense variants, which had not been reported in ExAC/gnomAD and
193 involved amino acid residues located in regions highly constrained for variation
194 ([Supplementary Table 1](#), [Supplementary Figure 2b](#)). No additional candidate variants
195 in clinically associated genes were identified in any patients (WES statistics and data

196 output are reported in [Supplementary Tables 2-6](#)). All affected residues were
197 conserved among ARF3 orthologs and paralogs and three of them were also
198 conserved among other RAS GTPases ([Supplementary Figure 2a](#)). The identified
199 missense variants affected residues whose corresponding positions in other GTPases
200 of the RAS superfamily had previously been associated with human disease
201 ([Supplementary Table 7](#)). The same Lys-to-Glu substitution at codon 127 in Subject 1
202 was recently reported to affect the corresponding residue in ARF1 in a patient with DD,
203 microcephaly, periventricular heterotopia, progressive cerebral atrophy and epilepsy³⁴.
204 Of note, this amino acid is homologous to Lys¹¹⁷ in HRAS (MIM: 190020), and an
205 activating missense variant of this residue in HRAS was reported in Costello syndrome
206 (CS [MIM: 218040])³⁶. Pro⁴⁷ (mutated in Subject 3) is homologous to Pro³⁴ in HRAS,
207 KRAS and NRAS ([Supplementary Figure 2a](#)). The same Pro-to-Ser change have
208 previously been reported as a somatic event in HRAS in vascular tumors³⁷, and
209 changes affecting Pro³⁴ in KRAS, HRAS and NRAS have been described in
210 RASopathies³⁸⁻⁴⁰(ClinVar). Moreover, a missense change affecting the adjacent
211 residue in ARF1 (p.Thr48Ile) was observed in a patient with clinical features
212 overlapping with the present series⁴⁰. In HRAS and KRAS, mutations affecting Thr⁵⁸,
213 which is adjacent to the aspartic acid residue homologous to Asp⁶⁷ in ARF3 (mutated
214 in Subject 2), have causally been linked to RASopathies^{38,41,42}. Finally, amino acid
215 substitutions at these residues in ARF3, its paralogs and members of the RAS
216 subfamily have been observed as somatic events in malignancies, providing further
217 evidence of their functional and clinical relevance ([Supplementary Table 7](#)).

218 Affected subjects showed variable degree of DD>ID ([Table 1](#), [Supplementary clinical](#)
219 [reports](#)). No characteristic craniofacial gestalt was noted, with only minor craniofacial

220 features reported, which were mainly related to microcephaly. Likewise Subject 1,
221 Subject 2 showed microcephaly, profound DD, progressive diffuse cortical atrophy with
222 diminished hemispheric white matter, with a thin corpus callosum, progressive
223 pontocerebellar hypoplasia, hypotonia, microsomia, and skeletal defects. A
224 comparable condition was also observed in Subjects 3 and 4, who manifested
225 hypotonia, variable DD>ID, microcephaly, and various MRI anomalies ([Table 1](#)). In
226 Subject 5, global DD and cognitive deficits were associated with hypoplasia of the
227 corpus callosum and mild white matter involvement in periventricular and
228 supraventricular areas, with normal head circumference ([Supplementary Figure 1](#)).
229 Early-onset seizures had been reported in Subjects 1 and 3.

230 **Disease-associated ARF3 variants variably affect protein stability and function**

231 The identified disease-associated variants affected residues spotted throughout the
232 coding sequence with exception of the C-terminus region ([Figure 1a](#)). First, we
233 investigated the functional consequences of each amino acid substitution by using a
234 three-dimensional structure of the GTPase recently solved by X-ray diffraction⁴³. We
235 noted that all residues cluster within or close to the GTP/GDP binding pocket ([Figure](#)
236 [1b](#)). Specifically, Lys¹²⁷ is one of the four residues of the NKXD motif directly mediating
237 binding to GTP/GDP by binding to the ribose ring¹⁶, and substitution of the positively
238 charged residue with a negatively charge glutamate was predicted to affect proper
239 nucleotide binding ([Figure 1c](#)). Similarly, Thr³² contributes to stabilize the GTP/GDP
240 binding via direct hydrogen bonding with one oxygen atom of the α phosphate ([Figure](#)
241 [1c](#)). While conservative, the Thr to Asn substitution was predicted to result in a steric
242 hindrance. Asp⁹³ does not directly contact GTP, even though it participates to the
243 overall general structure of the nucleotide binding pocket by a direct hydrogen bond

with the lateral chain of Lys¹²⁷ (Figure 1d). Since the high GTP:GDP ratio within cells, these three changes were anticipated to favor an active, GTP-bound state of the GTPase, bypassing the requirement for a GEF, as previously reported for pathogenic mutations affecting RAS proteins^{44,45}. On the other hand, Pro⁴⁷ and Asp⁶⁷ were predicted to affect ARF3 GTPase activity. Specifically, Pro⁴⁷ is located within the switch 1 region, which plays a key role in the catalytic activity of the GTPase and the conformational rearrangement mediating binding to effectors^{12,16}. Substitution of this non-polar residue with a polar serine is expected to strongly perturb the functional behavior of the protein. Similarly, Asp⁶⁷ participates in the coordination of the Mg²⁺ ion through direct hydrogen bonds with a water molecule¹⁵ (Figure 1c), and contributes to the regulation of GDP/GTP binding upon the “inter-switch toggle” mechanism⁴⁶; its substitution with valine was predicted to considerably perturb the GTP/GDP binding switch¹⁷ and the overall organization of the nucleotide binding pocket. No obvious consequence was hypothesized for the substitution involving Leu¹² (found in *cis* with p.Asp67Val in Subject 2) which resides in the flexible N-terminal domain of the GTPase. Of note, while Thr³², Asp⁹³ and Lys¹²⁷ map regions of the GTPase not directly involved in intermolecular contacts, Pro⁴⁷ and Asp⁶⁷ lie in regions close to the surface of the GTPase interacting with effectors/regulators⁴⁷, which does not rule out the possibility of a more complex functional behavior of the p.Pro47Ser and p.Asp67Val changes. To explore the structural and functional consequences of these two amino acid substitutions, we built a model of ARF3 interacting with the cytosolic coat protein complex (COP) formed by γ -COP (COPG1) and ζ -COP (COPZ1) starting from an available GTP-bound ARF1:COPG1-COPZ1 complex (PDB: 3TJZ) as template⁴⁸. The model for the wild-type (WT) ARF3 protein was validated by a 500-ns molecular dynamics (MD) simulation, documenting conservation of all known interactions with

269 GTP and Mg²⁺ (Figure 1d,e; Supplementary Table 8). The ARF3:COPG1 interface is
270 stabilized by an intermolecular hydrogen bonding network involving Arg¹⁹, Thr⁴⁸ and
271 Asn⁸⁴ ARF3 residues (Supplementary Table 9). We assessed the structural
272 perturbations due to the introduced p.Pro47Ser and p.Asp67Val changes using the
273 same time-frame. A minor impact on the ARF3 surface interacting with COPG1 was
274 evident in the simulation when introducing the Asp67Val substitution (Figure 1f;
275 Supplementary Table 9). As predicted by the structural inspection, this change resulted
276 instead in a significant rearrangement of the nucleotide binding pocket with a reduction
277 of the interactions of Lys¹²⁷ and Thr⁴⁵ with GTP (Supplementary Table 8). The Pro-to-
278 Ser substitution at codon 47 did not significantly affect ARF3 binding to GTP
279 (Supplementary Table 8), while a dramatic perturbation of the intermolecular binding
280 network with COPG1 due to a substantial rearrangement of the Switch 1 region was
281 observed (Figure 1g; Supplementary Table 9). Consistently, essential dynamics
282 analysis documented a major effect of Pro47Ser in terms of global fluctuations and
283 long range correlated movements, compared to the other simulations (Supplementary
284 Figure 3). Overall, the structural analyses predicted that all variants but p.Lys12Val
285 affect GTP/GDP binding and/or the GTPase activity of the protein, promoting an overall
286 stabilization of ARF3 in its catalytically active conformation. A more articulated impact
287 on conformational rearrangements mediating binding to effectors was suggested for
288 p.Pro47Ser.

289 To experimentally validate the predicted consequences of the identified variants on
290 ARF3 function, we investigated the biochemical behavior of a subset of mutants (*i.e.*,
291 ARF3^{P47S}, ARF3^{L12V;D67V} and ARF3^{K127E}) *in vitro*. First, we examined the protein levels
292 of the selected ARF3 mutants in transiently transfected COS-1 cells. Immunoblotting

293 analysis documented that ARF3^{P47S} level was comparable to the WT protein, while we
294 observed a considerably reduced level for both the ARF3^{K127E} and ARF3^{L12V;D67V}
295 mutants (Figure 2a), which was confirmed also *in vivo* (Supplementary Figure 4).
296 Treatment with the proteasome inhibitor MG132 and the autophagy inhibitor
297 bafilomycin A1 partially restored the levels of both mutants, indicating a reduced
298 stability and accelerated degradation (Figure 2b).

299 In its active GTP-bound state, ARF3 is able to bind to the Golgi-associated gamma-
300 adaptin ear-containing ARF-binding protein 3 (GGA3) to regulate downstream events
301 controlling *trans*-Golgi function and intracellular trafficking⁴⁹. Thereby, we performed
302 pull-down experiments using the GGA3 protein-binding domain (PBD) on cell lysates
303 to compare the relative amounts of GTP-bound fraction of WT and mutant ARF3
304 proteins and their ability to transduce signaling through proper binding to effectors.
305 Immunoblot analysis revealed a basal increase of the GTP-bound fraction for all
306 mutants compared to WT ARF3, which was statistically significant for ARF3^{K127E} and
307 ARF3^{L12V;D67V} (Figure 2c). These data are consistent with the MD predictions and
308 indicate a stabilized GTP-bound conformation and an overall hyperactive behavior of
309 the microcephaly-associated variants.

310 **Golgi integrity is altered in cells expressing the disease-associated ARF3
311 mutants**

312 The intracellular localization of ARF proteins is highly dynamic. GTP-bound ARF3
313 specifically localizes at the *trans*-Golgi, where it coordinates vesicle budding^{14,50}. Based
314 on these considerations and previous observations indicating the relevant role of ARF
315 proteins in maintaining proper organization and function of GA^{4,28,51}, we examined the
316 subcellular distribution of C-terminal mCherry-tagged ARF3 mutants and evaluated the

317 morphology of the *trans*-Golgi compartment using EGFP-tagged galactosidase T
318 (GaLT) as a marker⁵², in transfected COS-1 cells and zebrafish embryos (Figure 3a).
319 As expected, live cell imaging by confocal microscopy documented a diffuse
320 localization of WT ARF3 in cells (GDP-bound ARF3) already from ~4 hours after
321 transfection, and its co-localization with EGFP-GaLT (GTP-bound ARF3), which
322 showed a compact morphology of the intact *trans*-Golgi (Figure 3b; Supplementary
323 Video 1). In striking contrast, cells overexpressing ARF3^{K127E} were characterized by a
324 dispersed EGFP-GaLT signal over time (Figure 3c; Supplementary Video 1), indicating
325 a fragmentation of the *trans*-Golgi structure. This finding was confirmed by analyzing
326 fixed cells overexpressing ARF3^{K127E} also 24 hours after transfection by
327 immunofluorescence analysis against golgin 97, whose staining appeared weak and
328 dispersed compared to what observed in cells overexpressing WT ARF3
329 (Supplementary Figure 5a,b). Double labeling experiments and quantitative analysis
330 were extended to other ARF3 mutants, which confirmed a variable scattered/absent
331 golgin 97 signal, compared to the perinuclear compact and intense staining
332 documented in cells expressing the WT protein (Supplementary Figure 5c,d).
333 Fragmented *trans*-Golgi was observed in all the examined cells expressing ARF3^{K127E}
334 and ARF3^{L12V;D67V} and in a relevant proportion of cells expressing ARF3^{P47S}
335 (approximately 40%) (Supplementary Figure 5e). To further validate these findings *in*
336 *vivo*, we microinjected WT and mutant mCherry-tagged ARF3 mRNAs in zebrafish
337 embryos at the one-cell stage and assessed protein intracellular localization in
338 superficial cells (envelope layer cells, ELC) of early gastrula (Figure 3a,d,e). Consistent
339 with the *in vitro* findings, we observed a diffused distribution of WT ARF3 in cells, which
340 partially overlapped with EGFP-GaLT staining (Figure 3d). Conversely, ARF3^{K127E}
341 distribution in cells appeared markedly restricted, organized in small puncta, and co-

342 localized with EGFP-GaIT ([Figure 3e](#)), providing evidence of a strict localization at the
343 *trans*-Golgi and thereby of a stabilized GTP-bound state of the mutant protein.
344 Confirming the *in vitro* observations, differently from what observed in ELC cells in
345 embryos overexpressing WT mCherry-tagged ARF3, EGFP-GaIT staining appeared
346 reduced and more scattered (with an increase of cells showing “puncta” morphology)
347 in embryos injected with $ARF3^{K127E}$ mRNA, suggesting *trans*-Golgi fragmentation
348 ([Figure 3e, yellow arrows, Supplementary Figure 6](#)). Overall, these data suggest that
349 the p.Lys127Glu and p.Leu12Val;p.Asp67Val changes force ARF3 into a GTP-locked
350 (active) state, promoting a stable binding of the GTPase to the *trans*-Golgi membrane
351 that, in turn, affects Golgi integrity, resembling what previously observed for a
352 constitutively active (GTP-bound) ARF1 mutant⁵¹. To a minor extent, this effect was
353 also documented for the ARF3^{P47S} mutant.

354 **Expression of $ARF3^{K127E}$ and $ARF3^{L12V;D67V}$ in zebrafish embryos causes
355 pleiotropic effects on development and recapitulates the microcephalic trait**
356 Next, we analyzed the impact of the disease-associated missense changes in early
357 zebrafish development. WT and mutant myc-tagged ARF3 mRNAs were microinjected
358 together with the membrane marker GFP-CAAX mRNA at one cell stage
359 ([Supplementary Figure 7a](#)). Few hours after injection, embryos in their cleavage period
360 were sorted based on the expression of GFP-CAAX ([Supplementary Figure 7b, left](#)),
361 and developmental progression was followed from early time points of gastrulation till
362 48 hpf embryos (long-pec stage), when morphogenesis is nearly completed and sub-
363 compartmentalization of different neural structures can be appreciated⁵³. Upon
364 standard rearing conditions, we observed a statistically significant decrease in the
365 survival rate of embryos expressing each mutant at 24 hpf and 48 hpf, compared to

366 those expressing WT ARF3 and their not-injected siblings ([Supplementary Figure 7b](#),
367 right), with the strongest effect observed for ARF3^{K127E}. Development appeared
368 perturbed both at the level of the head and trunk ([Supplementary Figure 7c-e](#)). At 24
369 hpf, the severe phenotype (presence of microcephaly, microphthalmia, defective body
370 elongation and severe lateral bending) was highly prevalent in embryos expressing
371 ARF3^{K127E} (45.4%) ([Supplementary Figure 7c',e](#)), and occurred in a small proportion
372 of embryos expressing the ARF3^{L12V;D67V} mutant (3.8%) ([Supplementary Figure 7c'',e](#)).
373 While a negligible fraction of embryos expressing the WT protein (4.3%) was mildly
374 affected, this proportion was significantly higher in fish expressing each mutant (74%,
375 ARF3^{K127E}; 27%, ARF3^{L12V;D67V}) ([Supplementary Figure 7e](#)). A similar incidence was
376 observed even halving the concentration of injected ARF mutant mRNAs
377 ([Supplementary Figure 8a](#)). The phenotype worsened with time for both mutants, with
378 the most severe cases reaching 57% for ARF3^{K127E} and 17% for ARF3^{L12V;D67V} by the
379 time of hatching (48 hpf) ([Supplementary Figure 8b, c](#)).

380 When analyzed at 48 hpf, microcephaly was evident in zebrafish expressing mutant
381 ARF3 alleles ([Figure 4a-c'](#)). Indeed, embryos injected with ARF3^{K127E} and
382 ARF3^{L12V;D67V} mRNAs showed a significant reduction of the head area compared to
383 animals expressing WT ARF3 and not injected controls, with the most severe cases
384 lacking the frontal part of the brain and eyes ([Figure 4a,c](#)), as observed already at 24
385 hpf ([Supplementary Figure 7d,d'](#)). To validate the significance of the observed head
386 reduction, next we injected ARF3^{WT} and ARF3^{K127E} mRNAs in the transgenic
387 *NBT:dsRed* line, labeling differentiated neurons ([Figure 4b](#)). Volumetric
388 reconstructions and measurements from live confocal z-stack acquisitions at 48 hpf
389 confirmed a significant reduction of the brain volume ([Figure 4b,c'](#)). Additional

390 volumetric measurements obtained from fixed specimens at 48 hpf by labeling mature
391 brain structures using anti-acetylated alpha-tubulin and anti-HuC/Elav antibodies
392 ([Supplementary Figure 9](#)) further confirmed the deleterious effect of the $ARF3^{K127E}$
393 allele on brain development.

394 Next, to investigate the developmental processes implicated in the body curvature
395 defects observed in the embryos expressing the ARF3 mutants, we analyzed the
396 morphology and development of the notochord, which is crucial to support the body
397 elongation along the anterior to posterior axis (AP) and for subsequent spine
398 formation⁵⁴. At 30-35 hpf, when notochord morphogenesis is almost concluded,
399 confocal imaging analysis documented the occurrence of multiple notochord
400 curvatures per embryo in animals expressing each of the two mutant mRNAs, which
401 were distributed throughout the AP axis and were characterized by bending of variable
402 degrees ([Figure 4d-f](#)). In agreement with the overall severity of the observed
403 phenotype, $ARF3^{K127E}$ showed a significant higher number of notochord curvatures.
404 On the other hand, quantification of the degree of bending (180°: normal; 179° \geq angle
405 \geq 110°: mild; angle \leq 109°: severe) documented equivalent involvement in embryos
406 expressing the two ARF mutants. No gross phenotype related to either brain or body
407 axis morphology and size was observed in embryos expressing WT ARF3 and in non-
408 injected control siblings. Overall, these data indicate that the severe reduction of the
409 head in animals expressing mutant ARF3 proteins is caused by an impaired brain
410 development, recapitulating patients' microcephaly and that the observed embryo
411 curvatures are due to a perturbed notochord development.

412 **$ARF3^{K127E}$ and $ARF3^{L12V;D67V}$ alter PCP-dependent processes in early zebrafish
413 development**

We investigated further the perturbed head-trunk morphogenesis by tracing back axes establishment in embryos expressing WT and mutant ARF3 proteins. First, we examined patterning and morphogenesis in animals in their segmentation period (15 hpf, 13-14 somites). During this period, forebrain, midbrain and hindbrain are discernible, the embryo AP and ML axes are already established, and the embryo actively elongates with the tail bud protruding together with somites formation. mRNA levels of *Krox20*, which is expressed in anterior cephalic domain (hindbrain rhombomeres) and *MyoD*, expressed at the level of the trunk paraxial mesoderm (developing somites), was assessed in whole-mount embryos by *In situ* hybridization (ISH) ([Figure 5a](#)). While proper patterning of cephalic hindbrain region and paraxial mesoderm was in place, we observed a significant perturbation of the AP and ML axes ([Figure 5b-f](#)), which are defects typically linked to alteration of planar cell polarity (PCP)-controlled processes^{55,56} and consistent with previous observations reported in fish embryos expressing mutant ARF1 proteins³³. In detail, compared to their control siblings, mutant fish showed a clear shortening of the AP length and an expansion of the paraxial tissue in the ML axis ([Figure 5b](#)). Morphometric analysis of the *Krox20* and *MyoD* mRNA spatial expression profiles revealed a significant reduction of the AP length in the mutant embryos ([Figure 5b,c](#)) and a significant enlargement of the ML axis was evident in embryos expressing ARF3^{K127E} ([Figure 5b,d,e](#)). Consistently, the number of somites in mutant embryos was also reduced ([Supplementary Figure 10](#)). For both AP and ML axes defects, severely affected embryos were more prevalent among those expressing ARF3^{K127E} ([Figure 5f](#)).

Shortening and alteration of the body axes normally depend upon defective gastrulation occurring early during embryogenesis. At this developmental stage, cells

undergo a complex series of movements converging towards the dorsal midline and extending anteriorly that are controlled by trafficking and asymmetrical positioning of PCP components^{55–57}. To clarify the mechanism by which overexpression of activating ARF3 proteins causes severe axes perturbation in zebrafish development, first we investigated possible extension defects by measuring animal elongation in embryos at around 13 hpf (Figure 6a). At this stage, as a result of correctly orchestrated gastrulation movements, brain thickenings and tail bud are visible at the very anterior and posterior end of the embryo, respectively⁵³. Compared to embryos injected with WT ARF3 mRNA, a statistically significant increase of the angle between the developed cephalic and caudal structures was observed in embryos expressing ARF3^{K127E} (Figure 6b,c), which is indicative of delayed extension cell movements. Of note, embryos expressing the two mutants showed a statistically significant difference in the extent of early body elongation, which was in line with the difference observed during later segmentation stage (15 hpf) and at 24 hpf. In addition, live confocal imaging performed during gastrulation in individual ARF3^{WT} or ARF3^{K127E}-mCherry expressing embryos documented delayed epiboly in animals expressing the ARF3 mutant (Figure 6d,e). We also observed defective gastrulation movements in embryos expressing ARF3^{K127E} during the entire time-lapse, resulting in defective head and tail bud formation by the end of the acquisition.

These findings suggest that compromised convergent extension movements resulting from ARF3^{K127E} overexpression during gastrulation lead to an impairment of PCP-dependent body axes establishment. Cells expressing the mutant appeared mostly round in shape, with a reduced number of protrusions, with respect to cells expressing the WT protein (close-up in Figure 6d,e and Figure 6f), suggesting the possibility of an

462 altered polarity establishment and cytoskeletal organization as a molecular event
463 contributing to the defective cell motility.

464

465 **Discussion**

466 Here we identify *de novo* activating missense variants of *ARF3* as the molecular event
467 underlying a neurodevelopmental condition characterized by microcephaly,
468 progressive cerebral atrophy, and DD>ID, with short stature and skeletal abnormalities
469 variably occurring as associated features. The phenotype of this disorder is
470 reminiscent of the condition caused by activating mutations in *ARF1*³⁴. Consistently,
471 we show that disease-causing *ARF3* variants are variably activating, stabilizing the
472 protein in its GTP-bound conformation. Importantly, we also document that these
473 dominantly acting amino acid substitutions affect Golgi integrity, and perturb brain
474 formation and embryonic axes development in a vertebrate model, tracing back their
475 first assessable effect to defective PCP-mediated cell motility in early precursor cells.

476 The small GTPases of the ARF family are highly conserved across eukaryotes, occupy
477 different subcellular compartments involved in ER-GA network, and have both
478 redundant and distinct functions¹¹. These proteins control key molecular and cellular
479 processes, including targeted intracellular trafficking of signaling proteins, cell
480 migration and division, lipid metabolism, and signaling, which are important during
481 animal development^{1,32,33}. The intracellular localization and activity of ARF3 at the
482 *trans*-Golgi, where it promotes recruitment of coat complexes and vesicle formation, is
483 tightly regulated via a conformational switch controlled by reversible GDP-to-GTP
484 binding^{12,16}. By structural inspection, we demonstrated that disease-causing *ARF3*
485 mutations affect conserved residues involved in GDP/GTP binding/exchange, and pull-

486 down assays experimentally confirmed that two of the three tested mutants stabilize
487 the GTP-bound conformation of the protein, similarly to what has previously been
488 observed for other small monomeric GTPases of the RAS superfamily (e.g., ARF1,
489 HRAS, KRAS, NRAS, MRAS, RRAS, RRAS2) implicated in human disease^{34,58–}
490 ⁶³(COSMIC database). The functional relevance of this perturbed equilibrium between
491 the inactive and active state of the GTPase was further evidenced *in vivo* by
492 documenting a strict localization of the ARF3^{K127E} protein at the *trans*-Golgi in zebrafish
493 embryos. It should be mentioned that two mutations (p.Pro47Ser and p.Asp67Val)
494 affected a conserved hydrophobic region involved in effector binding^{17,64,65}, with
495 molecular dynamics simulations suggesting a major perturbation exerted by the
496 p.Pro47Ser substitution on ARF3 binding to effectors. These considerations stimulate
497 future studies aimed to demonstrate whether effector binding in these mutants is
498 qualitatively and/or quantitatively altered.

499 ARF1 and ARF3 are known to play a key role in maintaining organelle integrity^{27,28,66}.
500 Xiang et al. (2007)⁵¹ showed that physiological GA fragmentation in mitotic cells is
501 principally mediated by the active form of ARF1 (GTP-bound), which triggers the
502 continued budding of COPI vesicles. Similarly, while depletion of ARF1 was not
503 reported to affect GA function¹¹, disruption of the GA network was observed in cells
504 expressing a constitutively active ARF1 mutant⁵¹, causing GA swelling with sustained
505 vesiculation¹³. Consistent with the role of these proteins in maintaining organelles
506 structural organization, live imaging in cells expressing the ARF3^{K127E} protein both *in*
507 *vitro* and during early zebrafish gastrulation documented a strong and rapid effect on
508 GA integrity, indicating that a shift of the equilibrium towards the GTP-bound form of
509 ARF3 dramatically affect *trans*-Golgi morphology and embryo development. The

510 molecular mechanism by which aberrant ARF3 function causes GA fragmentation and
511 whether this impacts vesicle biogenesis and trafficking remains to be determined.

512 The finding of fragmented GA in cells and embryos expressing the disease-associated
513 ARF3 mutants assigns this disorder to the recently defined family of “Golgopathies”, a
514 group of neurodevelopmental disorders clinically characterized by a wide spectrum of
515 central nervous system abnormalities^{8,9}. Similar to what was observed in the present
516 cohort, patients with activating *ARF1* pathogenic variants show DD/ID, microsomia,
517 microcephaly and brain abnormalities, including delayed myelination, cortical and
518 cerebellar atrophy, and seizures as major features. Different from what observed in the
519 present series, periventricular heterotopia is a recurrent feature in patients with
520 activating *ARF1* variants. A related but distinct neurodevelopmental disorder,
521 periventricular heterotopia with microcephaly (ARPHM, MIM: 608097), has been linked
522 to biallelic inactivating variants of *ARFGEF2*. This recessive disorder is characterized
523 by severe DD/ID, epilepsy, brain atrophy and delayed myelination associated with thin
524 corpus callosum⁶⁷. Together with previous findings, our work documents the critical
525 role of GA for diverse neurodevelopmental processes as well as for neuronal function.

526 Our *in vivo* results deepen the understanding on the impact of dominant *ARF3*
527 mutations on development. Post-Golgi cell trafficking and correct sorting of polarity
528 components are required for asymmetric cell division and migration in the vertebrate
529 brain, underlying neurogenesis, axon arborization and sustained synaptogenesis^{32,68}.
530 In line with this evidence and the features documented in patients with mutated *ARF3*
531 alleles, transient overexpression of the *ARF3*^{K127E} protein coupled to volumetric
532 imaging reconstruction and live cell analysis in zebrafish embryos revealed a clear
533 microcephalic trait and occurrence of defects linked to altered PCP signaling during

534 early gastrulation.

535 Convergence and extension movements, which require a fine tuning of cell polarity
536 mechanisms and are needed to shape the AP and ML axes and proper head and trunk
537 domains⁵⁶, were evidently affected in animals expressing the ARF3 mutants.
538 Biosynthetic trafficking and a correct function of ER and GA is essential during animal
539 development for regulating morphogens' distribution^{32,33,69}, which include components
540 of the PCP pathway and cadherins required for cell polarity establishment and
541 migration, as shown *in vitro*⁷⁰, nematodes⁷¹ and zebrafish⁷². Consistent with our
542 findings, fish expressing the hyperactive microcephaly-associated ARF1 mutant show
543 PCP-related axial defects³³, and fish mutants for ARF-interacting COPI/COPII coat
544 components exhibit skeletal and notochord abnormalities with GA disruption^{73,74}. Of
545 note, the impaired function of ARFGEF2 underlying the microcephalic traits observed
546 in patients with ARPHM, has been linked to proliferative and migratory defects due to
547 *trans*-Golgi to membrane trafficking of E-cadherins and beta-catenin⁷⁵. Altogether, this
548 body of evidence points to an important role of ARF-mediated trafficking of signaling
549 components during brain and body plan development deserving further investigation.

550 In conclusion, our findings highlight a role of ARF3 in the maintenance of *trans*-Golgi
551 integrity, and document an obligate dependence of early developmental processes and
552 brain morphogenesis on proper function of this GTPase, identifying *ARF3* as a novel
553 gene implicated, when mutated, in a neurodevelopmental disorder belonging to the
554 emerging class of "Golgipathies"^{8,9}. Further studies are required to understand how
555 ARF3-driven disruption of GA integrity impacts developmental signaling homeostasis
556 throughout embryogenesis, and thereby the cellular processes underlying brain
557 formation.

558 **Methods**

559 **Subjects**

560 The study has been approved by the local Institutional Ethical Committee of the
561 Ospedale Pediatrico Bambino Gesù IRCCS (OPBG), Rome (1702_OPBG_2018).
562 Subject 1 was analyzed in the frame of a research project dedicated to undiagnosed
563 disorders (Undiagnosed Patients Program, OPBG), while the other subjects were
564 referred for diagnostic genetic testing. Clinical data and DNA samples were collected,
565 stored and used following procedures in accordance with the ethical standards of the
566 declaration of Helsinki protocols, and after signed consents from the participating
567 families. Permission was obtained to publish photographs of Subjects 1 and 4.

568 **Exome sequencing analysis**

569 In all families, whole-exome sequencing (WES) was performed using DNA samples
570 obtained from leukocytes and a trio-based strategy was used. Target enrichment kits,
571 sequencing platforms, data analysis, and WES statistics are reported in
572 [Supplementary Table 2-6](#) and in the [Supplementary Methods](#). WES data processing,
573 read alignment to the GRCh37/hg19 version of genome assembly, and variant filtering
574 and prioritization by allele frequency, predicted functional impact, and inheritance
575 models were performed as previously reported⁷⁶⁻⁸⁰. WES data output is summarized
576 in [Supplementary Table 2-6](#). Cloning of the genomic portion encompassing the
577 c.34C>G and c.200A>T missense substitutions (p.Leu12Val and p.Asp67Val; Subject
578 3) was used to confirm that both variants were on the same allele. Variant validation
579 and segregation were assessed by Sanger sequencing in all the subjects included in
580 the study.

581 **Structural analysis and molecular dynamics simulations**

582 The structural impact of the disease-associated missense changes was assessed
583 using the available three-dimensional structures of human ARF3 complexed with GTP
584 and *V. vulnificus* multifunctional-autoprocessing repeats-in-toxin (MARTX) (PDB
585 6ii6)⁴³. The structure was visualized using the VMD visualization software⁸¹.

586 A model of GTP-bound ARF3 interacting with the cytosolic coat protein complex
587 subunits γ -COP (COPG1) and ζ -COP (COPZ1) was built using the SWISS-MODEL
588 automated protein structure homology modelling server
589 (<http://swissmodel.expasy.org>)⁸² using the 2.90 Å resolution X-ray structure (PDB
590 3TJZ)⁴⁸. Alignment of template and model amino acid sequences is reported in
591 [Supplementary Figure 11](#). The p.Asp67Val and p.Pro47Ser mutations were introduced
592 using the UCSF Chimera package⁸³. The side-chain orientations were obtained with
593 the Dunbrack backbone-dependent rotamer library⁸⁴, choosing the best rotamer with
594 minimal/no steric clashes with neighboring residues. Following protonation of titratable
595 amino acids at pH=7, proteins were added in cubic boxes and solvated in water.
596 Counter-ions were added to neutralize the charges of the system with the genion
597 GROMACS tool⁸⁵. After energy minimizations, the systems were slowly relaxed for 5
598 ns by applying positional restraints of 1000 kJ mol⁻¹ nm⁻² to atoms. Unrestrained
599 simulations were carried out for a length of 500 ns with a time step of 2 fs using
600 GROMACS 2020.2. The CHARMM36 all-atom force field⁸⁶ was used for the protein
601 description and water molecules were described by TIP3P model¹⁰⁴. V-rescale
602 temperature coupling was employed to keep the temperature constant at 300 K⁸⁷. The
603 Particle-Mesh Ewald method was used for the treatment of the long-range electrostatic

604 interactions⁸⁸. The first 5 ns portion of the trajectory was excluded from the analysis.
605 All analyses were performed using GROMACS utilities.

606 **Expression constructs and *in vitro* mRNA synthesis**

607 The full-length coding sequence of WT human ARF3 (NM_001659.3) was obtained by
608 PCR and cloned into the pcDNA3.1/myc-6His eukaryotic expression vector (Life
609 Technologies). The disease-associated substitutions were introduced by site-directed
610 mutagenesis (QuikChange II Site-Directed Mutagenesis Kit, Agilent Technologies). For
611 zebrafish expression experiments, the myc-tagged (C-terminus) WT and mutant ARF3
612 sequences were subcloned into the pCS-Dest vector (plasmid 22423, Addgene)⁸⁹ via
613 LR clonase-mediated recombination (ThermoFisher). pCS-Dest-mKOP2-CAAX and
614 pCS-Dest-EGFP-GalT were generated by subcloning the Addgene plasmids 75155⁹⁰
615 and 11929⁹¹, respectively. Plasmids were digested and linearized with *Kpn*I (NEB New
616 England Biolabs), and mRNA was produced using mMessage mMachine SP6
617 transcription kit and poly(A) tailing kit (Thermo Fisher). The GFP-CAAX expressing
618 plasmid was a gift from Dr. M. Handberg Thorsager. For live confocal experiments,
619 pcDNA3/hARF3(WT)-mCherry (plasmid 79420, Addgene)⁹² was used and subcloned
620 into zebrafish pCS-Dest vector. All cloned sequences were confirmed by bidirectional
621 DNA sequencing.

622 **COS-1 cell culture and transient transfection assays**

623 COS-1 cells were cultured in Dulbecco's modified Eagle's medium supplemented with
624 10% heat-inactivated fetal bovine serum (GIBCO), 1x sodium pyruvate and 1x
625 penicillin-streptomycin, at 37 °C with 5% CO₂. Subconfluent cells were transfected with
626 myc- or mCherry-tagged WT and mutant ARF3 expressing vectors using FuGENE 6
627 (Promega), according to the manufacturer's instructions.

628 **ARF3-myc immunoblotting**

629 Transfected COS-1 cells were lysed in radio-immunoprecipitation assay (RIPA) buffer,
630 pH 8.0, containing phosphatase and protease inhibitors (Sigma-Aldrich). Lysates were
631 kept on ice for 30 min and centrifuged at 16,000 g for 20 min at 4 °C. Samples
632 containing an equal amount of total proteins (15 µg) were resolved by 12% sodium
633 dodecyl sulfate (SDS)-polyacrylamide gel (Biorad). Proteins were transferred to
634 nitrocellulose membrane using a dry transfer system (Biorad), and blots were blocked
635 with 5% non-fat milk powder (Biorad) in Phosphate-buffered saline (PBS) containing
636 0.1% Tween-20 for 1 h at 4 °C and incubated with mouse monoclonal anti-myc (1:1000,
637 Cell Signaling), mouse monoclonal anti-β-tubulin (1:1000, Sigma-Aldrich) and anti-
638 mouse HRP-conjugated secondary antibody (1:3000; Sigma). Pools of zebrafish
639 embryos ($n = 30$) were collected stored dry (-80 °C) at gastrula (6 hpf) and
640 segmentation stage (15 hpf). Lysates from non-injected control embryos and those
641 injected with myc-tagged ARF3^{WT}, ARF3^{K127E} and ARF3^{L12V;D67V} were obtained by
642 syringe homogenization in lysis buffer (Tris HCl 10 mM pH 7.4; EDTA 2 mM; NaCl 150
643 mM; Triton X-100 1% with 1X protein inhibitors cocktail (Roche) and equal amounts of
644 protein extracts (40 µg) were separated on a 12% Sodium dodecyl sulfate (SDS)-
645 polyacrylamide gel. The total protein concentration was determined by the Bradford
646 assay (Bio-Rad) using Cary 100 UV-Vis (Agilent Technologies). After electrophoresis,
647 the proteins were transferred to PVDF membrane (Bio-Rad) using a wet transfer
648 system (Biorad). Blots were blocked with 5% non-fat milk powder (Biorad) or bovine
649 serum albumin (Sigma-Aldrich) in PBS containing 0.1% Tween-20 overnight at 4°C
650 constantly shaking and incubated with primary antibody in blocking solution. The
651 following primary antibodies were used: mouse monoclonal anti-myc (Cell Signaling,

652 dilution 1:1000), rabbit polyclonal anti-GAPDH (Genetex, dilution 1:1000). Following
653 washes in PBST 0.1%, membranes were incubated with anti-mouse and anti-rabbit-
654 HRP-conjugated secondary antibodies (1:3000) (Sigma). Immunoreactive proteins
655 were detected by an enhanced chemiluminescence (ECL) detection kit (Thermo
656 Fisher) according to the manufacturer's instructions, and an Alliance Mini HD9 was
657 used for chemiluminescence detection (Uvitec).

658 **ARF3 protein stability assays**

659 COS-1 cells were seeded at 3×10^5 in 6-well plates and the following day were
660 transfected with WT or mutant myc-tagged *ARF3* expression constructs for 24 hours.
661 A subset of transfected cells was then treated with proteasome inhibitor MG132 (100
662 μM) or with the autophagy inhibitor bafilomycin A1 (200 nM) (Sigma-Aldrich) for 6
663 hours.

664 **ARF3 activation assay**

665 COS-1 cells (1×10^6) were seeded in 100 mm petri dishes and transfected with myc-
666 tagged *ARF3* expression constructs. Twenty-four hours after transfection, cells were
667 washed twice with ice cold PBS and collected in 50 mM Tris (pH 7.4), 150 mM NaCl,
668 10mM MgCl₂, 10% Glycerol, 1% NP-40 with proteases and phosphatase inhibitors
669 (Sigma-Aldrich). Cell lysates were further subjected to pull-down using GGA3-
670 conjugated agarose beads (Cell Biolabs) and incubated at 4 °C for 60 min. For
671 immunoblotting analyses, pulled down samples and whole cell lysates were combined
672 with a 2x sample buffer and denatured at 95 °C for 5 min. Samples were then
673 separated by SDS-PAGE and incubated with anti-myc and anti-β-tubulin antibodies.
674 GTP-bound protein level was detected by an ECL detection kit (Thermo Fisher).

675 **ARF3 protein localization and Golgi morphology assessment in fixed COS-1
676 cells**

677 COS-1 cells (30×10^3) were seeded in 24-well cluster plates onto 12-mm cover glasses
678 and transfected with WT or mutant mCherry-tagged *ARF3* expression constructs for
679 24 hours. Cells were then fixed with 3% paraformaldehyde for 30 minutes at 4 °C,
680 followed by permeabilization with 0.5% Triton X-100 for 5 minutes at room temperature.
681 Cells were stained with mouse monoclonal anti-Golgin 97 antibody (1:50, Abcam) for
682 1 hour at room temperature, rinsed twice with PBS and incubated with Alexa Fluor 488
683 goat anti-mouse secondary antibody (1:200, Molecular Probes) for 1 hour at room
684 temperature. After staining, coverslips were mounted on slides by using Vectashield
685 Antifade mounting medium (Vector Laboratories) containing 1.5 µg/ml DAPI (Sigma).
686 Images were acquired using Olympus Fluoview FV1000 confocal microscope using
687 60x/1.42 oil objective and signals from different fluorescent probes were taken in
688 sequential scanning mode. Cells were screened for incidence of Golgi phenotype.

689 **Time-lapse imaging of Golgi dynamics in COS-1 cells expressing ARF3**

690 For live imaging, COS-1 cells (10×10^4) were seeded into µ-dishes 35 mm (Ibidi)
691 24 hours before transfection. The day after, cells were co-transfected with WT or
692 mutant mCherry-tagged *ARF3* and EGFP-GaT constructs. Four hours post-
693 transfection, time-lapse acquisitions were performed with a Leica TCS-SP8X confocal
694 microscope (Leica Microsystems) with a PL Apo CS2 20x/0.75 objective. Z-
695 reconstructions of serial single optical sections were obtained every 15 min and carried
696 out with a 1024x1024 format, scan speed of 600Hz, a zoom magnification up to 1.5
697 and z-step size of 0.7 µm. Live imaging of samples was performed simultaneously
698 using the Mark & Find mode of the LAS X software. Time-lapse microscopy was

699 performed with a stage incubator (OkoLab) allowing to maintain stable conditions of
700 temperature, CO₂ and humidity during live cell imaging.

701 **Zebrafish husbandry**

702 Zebrafish NHGRI-1⁹³ and Tg(NBT: dsRed)⁹⁴ were cultured following standard
703 protocols⁹⁵. Fish were housed in a water circulating system (Tecniplast) under
704 controlled conditions (light/dark 14:10, 28 °C, 350-400 uS, pH 6.8-7.2) and fed daily
705 with dry and live food. All experiments were approved by the Italian Ministry of Health
706 (23/2019-PR).

707 **Zebrafish mRNA microinjection**

708 Injection of *in vitro* synthesized capped mRNAs encoding myc-tagged ARF3 (7.5 and
709 15 pg), mCherry-tagged ARF3 (15 pg), mKOPF-CAAX (15 pg), H2A-mCherry (15 pg),
710 EGFP-GaIT (15 pg), EGFP-CAAX (15 pg) and EGFP-GaIT (50pg) was performed in
711 one-cell stage zebrafish embryos using FemtoJet 4x microinjection system
712 (Eppendorf). Injected embryos were cultured under standard conditions at 28 °C in
713 fresh E₃ medium and for each batch, non-injected fish were used as controls together
714 with fish injected with the WT form of ARF3 mRNA. Embryos were monitored every
715 day and survival rate was analyzed at 24 and 48 hours post-fertilization (hpf).

716 **Zebrafish body axis, notochord and head phenotyping**

717 Embryos were screened for gross phenotype penetrance classified as normal, mild
718 and severe at 24 hpf. For detailed analysis, not-injected controls and injected fish at
719 12 and 15 hpf (for body axis), 24 hpf (for notochord) and 48 hpf (for head size) were
720 embedded in 2% low melting agarose dissolved in E₃ medium. Bright-field images were
721 acquired at Leica M205FA microscope with 0.63x magnification (Leica Microsystems).

722 These parameters were assessed: i) angle between the antero-posterior ends (body
723 axis); ii) number of notochord curvatures and degree of the notochord angles (plotted
724 in a Rose diagram using Oriana)⁹⁶; iii) head size measured by the area surface
725 between the rostral most part of the head and the optic vesicle.

726 **Whole-mount immunofluorescence for acetylated α-tubulin and HuC/Elav in**
727 **zebrafish embryos**

728 Whole-mount samples were fixed in 4% paraformaldehyde (Thermo Fisher), washed
729 in PBS-Triton 0.8% (PBSTr 0.8%), permeabilized with proteinase K treatment (1 µg/ml)
730 and incubated in 2% blocking reagent (Roche) for 2 hours. Samples were then
731 incubated with the primary antibody in 2% blocking reagent overnight at 4 °C (anti
732 acetylated α-tubulin, 1:500, Sigma-Aldrich). After several washes in PBSTr 0.8%,
733 samples were incubated with the Alexa Fluor 488 goat anti-mouse secondary antibody
734 (1:1000, Thermo Fisher) overnight at 4 °C with gentle shaking. Whole-mount larval
735 samples were mounted in 90% glycerol. Dorsal z-stacks (volumes) of embryos stained
736 for acetylated α-tubulin were acquired with a Leica TCS-SP8X confocal microscope
737 with PL Apo CS2 20x/0.75 objective scanning with 1024 x 1024 format, speed of 400
738 Hz and z-step size of 2 µm. Embryos stained for HuC/Elav were imaged as above or
739 using Olympus FV1000, objective 20x/0.75 dry, with same parameters.

740 **Zebrafish live brain volume imaging and 3D rendering from *Tg(NBT:dsRed*) fish**
741 Live confocal acquisitions from 48 hpf injected *Tg(NBT:dsRed)* fish embedded in 2%
742 low melting agarose in E₃ medium were obtained with Leica Stellaris 5 confocal
743 microscope using hybrid detectors and keeping minimal laser power. Scans were
744 obtained with 512x 512 resolution, 400 Hz. Live z-stacks were acquired with Fluotar
745 25x/0.95 water-immersion objective and with a z-step size of 2.5 µm. Volumetric brain

746 reconstructions from representative 48 hpf injected *Tg(NBT:dsRed)* fish were obtained
747 using *3D Volume* (Blend model) and *Surfaces* rendering functions of Imaris (Bitplane),
748 employing the same parameters for the different individuals.

749 **Zebrafish brain volume analysis**

750 Anterior brain volume was measured on both live *Tg(NBT:dsRed)* embryos and fixed
751 specimens stained with antibodies against HuC/Elav and acetylated α-tubulin. A region
752 of interest (ROI) comprising the most anterior part of the *NBT:dsRed*+ neurons and the
753 cerebellum was selected along the whole z-stacks of the confocal 3D data using Fiji
754 analysis tools. Image data were binarized employing *Threshold/Otsu* and *B&W/Dark*
755 *background* algorithms. For every z-stack layer the surface area measurement was
756 extrapolated using a custom-made macro. Volumetric measurements were obtained
757 taking into account the x Z-step value.

758 **Whole-mount *in situ* hybridization of Krox20 and MyoD mRNA**

759 The fragments of *Krox-20* and *MyoD* cDNA used for riboprobe synthesis were amplified
760 from a zebrafish cDNA preparation by PCR using One Taq DNA polymerase (NEB
761 New England Biolabs) and the primers listed in [Supplementary Table 10](#). The PCR
762 fragments were cloned into pGEM-T Easy vector (Promega) and sequences were
763 confirmed by DNA sequencing. The digoxigenin-labeled antisense riboprobes were
764 synthesized by *in vitro* transcription with DIG RNA labeling kit SP6/T7 (Roche). *In situ*
765 hybridization analysis in whole-mount zebrafish embryos at 15 hpf was performed as
766 previously described⁹⁷. Briefly, samples were permeabilized with proteinase K
767 treatment (1 µg/ml) for 2 minutes, pre-incubated in 2% blocking reagent (Roche) and
768 incubated with riboprobes (2 ng/µl) in hybridization mix (50% formamide, 1.3x SSC,
769 100 g/ml heparin, 50 µg/ml yeast RNA, 0.2% Tween-20, 0.5% CHAPS, 5 mM EDTA

770 pH 8) at 65 °C for at least 15 hrs. Afterwards, samples were rinsed with scalar dilutions
771 of SSC solutions and incubated with anti-alkaline phosphatase (AP)-conjugated
772 antibody (1:5000, Roche) for 2 hours at room temperature. Chromogenic staining was
773 developed via BM Purple substrate (Roche) according to manufacturer's instructions.
774 Specimens were mounted in 90% glycerol and dorsal images were acquired from
775 Olympus TH4-200 microscope (Olympus Life Science) with 10x objective.

776 **Confocal live imaging of zebrafish embryos during gastrulation**

777 For *in vivo* imaging, embryos at mid-gastrula stage were embedded in 2% low melting
778 agarose dissolved in E₃ medium. 4D fluorescent data were acquired using Leica TCS-
779 SP8X confocal microscope using hybrid detectors, keeping minimal laser power.
780 Scans were obtained in a 1024 x 1024 format, with a speed of 400Hz. Fluorochromes
781 unmixing was performed by acquisition of automated-sequential collection of multi-
782 channel images, in order to reduce spectral crosstalk between channels, and the same
783 setting parameters were used for all examined samples. For ARF3 localization and
784 Golgi detection sequential confocal images were acquired with Fluotar 25x/0.95 water-
785 immersion objective with a z-step size of 2.5 μm. Gastrulation time-lapses were
786 acquired with a PI Apo CS2 20x/0.75 objective. Z-reconstructions of serial single optical
787 sections were obtained every 30 min with a z-step size of 3 μm. Embryo live imaging
788 was performed simultaneously using the Mark & Find mode of the LAS X software.

789 **Trans-Golgi fragmentation analysis in live zebrafish embryos**

790 Fragmented *trans*-Golgi morphology was assessed from single confocal images of the
791 animal pole of at 12 hpf embryos injected with ARF3^{WT} and ARF3^{K127E} GalT-GFP and
792 mKOFP-CAAX mRNA. Trans-Golgi morphology (GalT-GFP+) in each cell was scored
793 as "ribbon" if it displayed a recognizable circular and compact structure or "puncta" if it

794 displayed a clear fragmented pattern. Circa 30-40 cells per embryo were counted, n=

795 4 (ARF3^{WT}) and n = 5 ($\text{ARF3}^{\text{K127E}}$) embryos. Fisher's exact test in a 2x2 contingency

796 table (puncta vs. ribbon) (**** p < 0.0001) is used to assess statistical significance.

797 **Statistical analysis and Image processing**

798 Data were analyzed independently by at least two researchers and statistical

799 assessments were performed using GraphPad Prism. Log-rank (Mantel-Cox) test was

800 used to assess survival in zebrafish mutants. For phenotype penetrance assessment

801 Fisher's exact test in a 2x2 contingency table was used, performed as pairwise

802 statistical comparisons across experimental conditions (normal versus mild or severe

803 *in vivo* and compact versus fragmented Golgi morphology phenotype for *in vitro*

804 analyses). Normality tests (Anderson-Darling, D'Agostino & Pearson, Shapiro-Wilk and

805 Kolmogorov-Smirnov tests) were run to assess normal distribution of the data.

806 Parametric data with more experimental groups were analyzed with Anova test, non-

807 parametric data with Kruskal-Wallis test and specific *post hoc* tests were always used

808 as indicated in the figure legends. Whenever multiple measurements in zebrafish were

809 performed on the same individual (e.g., different cells from the same embryo), analysis

810 with a mixed-effects model were used to take account of resampling from the same

811 cluster (embryo). All the analyses were two-tailed. Outliers identification were

812 assessed by ROUT method (Q = 1%). An overview of the statistical analysis for each

813 dataset is shown in [Supplementary Table 11](#). Raw images were analyzed with Fiji⁹⁸,

814 LAS X Life Science imaging software (Leica Microsystem), FV10-ASW software,

815 Olympus CellSens Standard imaging software (Olympus Life Science) and Imaris

816 (Bitplane) and processed using Photoshop or Illustrator (Adobe Systems Incorporated)

817 for figure assembly. Brightness and contrast were adjusted equally across the whole
818 image.

819 **Supplemental data description**

820 The article includes the following supplemental data:
821 Supplementary Methods and clinical reports, 11 figures, 11 tables and 1 video (.mp4).

822 **Acknowledgments**

823 H2A-mCherry:pDest and GFP-CAAX:pDest plasmids were kindly provided by Dr.
824 Mette Handberg-Thorsager (Max Planck Institute of Molecular Cell Biology and
825 Genetics, Dresden, MPI-CBG, Germany). We acknowledge Cineca ELIXIR-IIB for
826 computing resources. This work was supported, in part, by Fondazione Bambino Gesù
827 (Vite Coraggiose to M.T.), Italian Ministry of Health (CCR-2017-23669081 and RCR-
828 2020-23670068_001 to M.T; RF-2018-12366931 to F.C.R., G.C. and B.D.; Ricerca
829 Corrente 2021 to A.L., S.C. and M.T., and RF-2013-02355240 to R.G.), Italian Ministry
830 of Research (FOE 2019 to M.T.), the Tuscany Region Call for Health 2018 (DECODE
831 EE, to R.G.), and the European Union Seventh Framework Programme (DESIRE
832 [602531] to R.G.).

833 **Authors'contribution**

834 G.F. designed and performed the *in vivo* experiments and contributed to write the
835 manuscript. V.M. designed and performed the *in vitro* experiments and contributed to
836 write the manuscript. F.C.R. coordinated the clinical data collection and phenotyping,
837 analyzed the clinical data and contributed to write the manuscript. L.A.C., S.P. and
838 S.C. performed the confocal scanning experiments. M.V. performed the *in situ*
839 hybridization assays. A.Z., A.V., F.P., S.P., A.B., and M.I. generated and analyzed the

840 genomic data. G.C., I.G.P. and B.C. performed the structural analyses and molecular
841 dynamics simulations. M.B., C.B., D.M., A.S., M.M., M.V.G., A.B., R.G., A.S. and B.D.
842 identified the patients, and collected and analyzed the clinical data. A.L. and M.T.
843 conceived, designed, supervised the project, analyzed the data, and wrote the
844 manuscript.

845

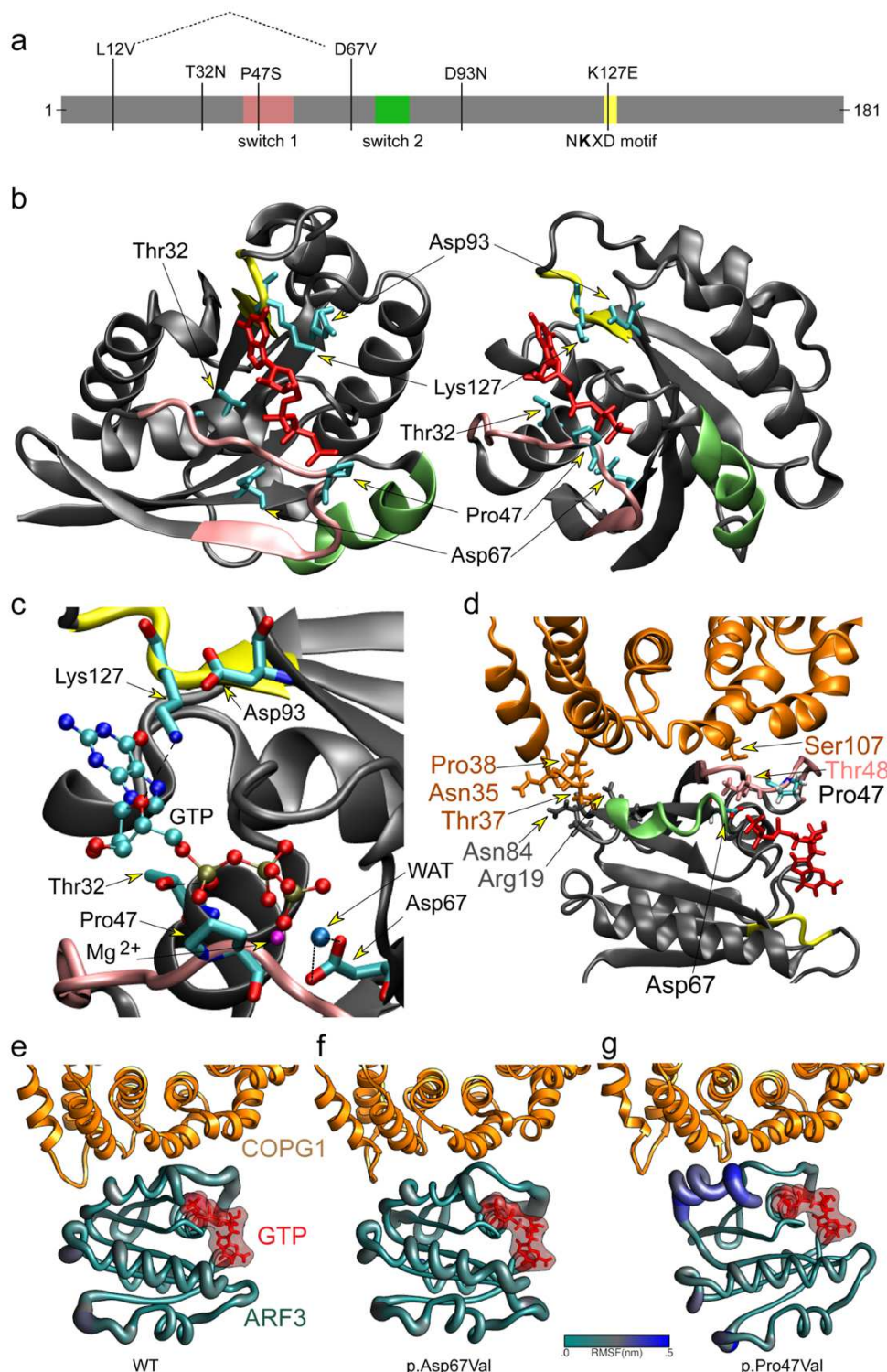
846 **Declaration of Interests**

847 The authors declare no competing interests.

848 **Data availability**

849 The data generated in this work are available upon request from the corresponding
850 authors.

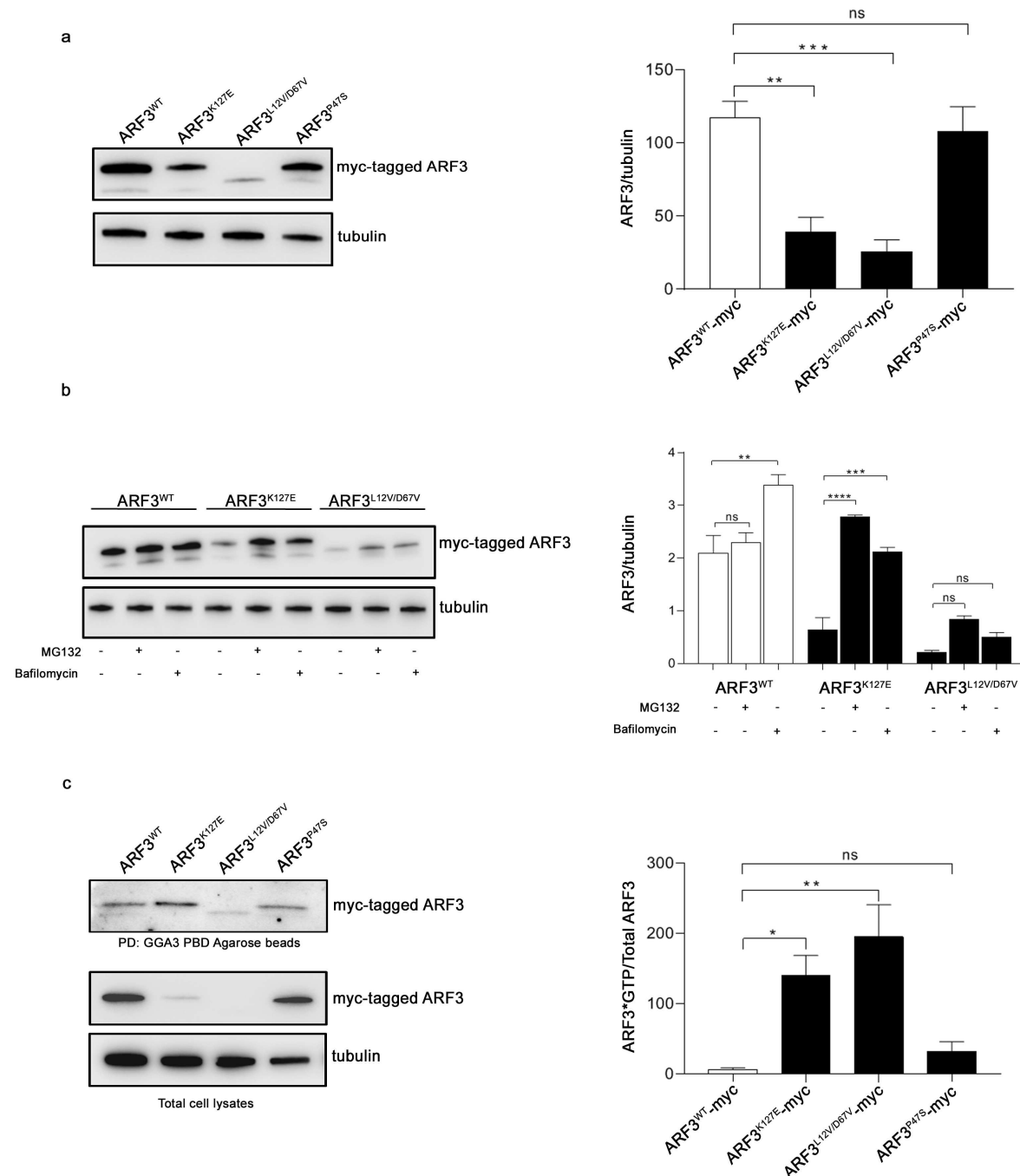
851 **Figures**



852

853 **Figure 1. Structural organization of ARF3, location of mutated residues and**
 854 **molecular dynamics analyses.** (a) Domain organization of ARF3 excluding the

855 unstructured C-terminal tail. Switch 1, switch 2 and the NKXD fingerpoint motif are
856 highlighted in pink, green and yellow, respectively. The variants identified in affected
857 subjects are also reported; **(b-c)** 3D structure in two different orientations of GTP-
858 bound ARF3 interacting with the MARTX toxin (PDB 6ii6). Side chains of the ARF3
859 residues mutated in the affected subjects and GTP are in cyan and red, respectively.
860 Main chain of residues belonging to switch 1, switch 2 and NKXD fingerpoint motif are
861 colored as above; **(d)** Enlargement of the ARF3 GTP binding pocket with the five
862 mutated residues. The direct hydrogen bond between the N atom in the Lys127 lateral
863 chain and the oxygen atom of the GTP ribose ring is highlighted in dashed line. The
864 Mg²⁺ ion is colored in magenta, while the oxygen atom of the water molecule, mediating
865 the interaction between Asp67 and the manganese ion, is shown in light blue color.
866 The two hydrogen bonds between Asp67 and the water molecule are highlighted with
867 dotted lines. **(e)** Homology model of GTP-bound ARF3 interacting with the cytosolic
868 coat protein complex COPG1-COPZ1 (PDB: 3TJZ) validated by a 500-ns molecular
869 dynamics (MD) simulation. The region of contact between ARF3 and COPG1 (orange
870 color) is shown in e. **(f-h)** MD simulations of wild-type (f), p.Asp67Val (g) and
871 p.Pro47Ser (h) ARF3 complexed with COPG1-COPZ1. Residues involved in the
872 contact are shown with their side chain and colored as the respective protein/region.
873 ARF3 backbone is represented with a diameter proportional to its per-residue
874 fluctuations (RMSF).

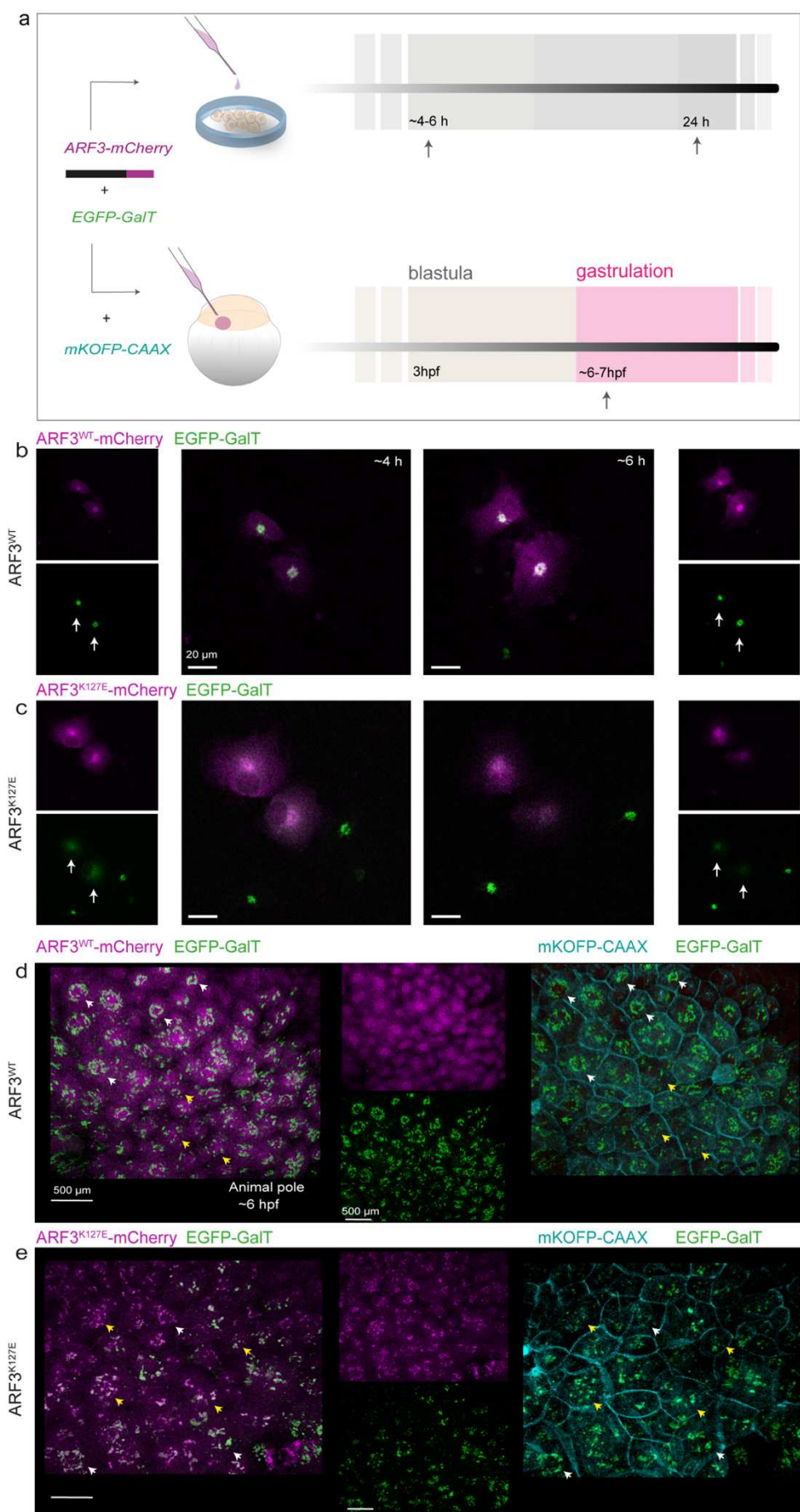


875

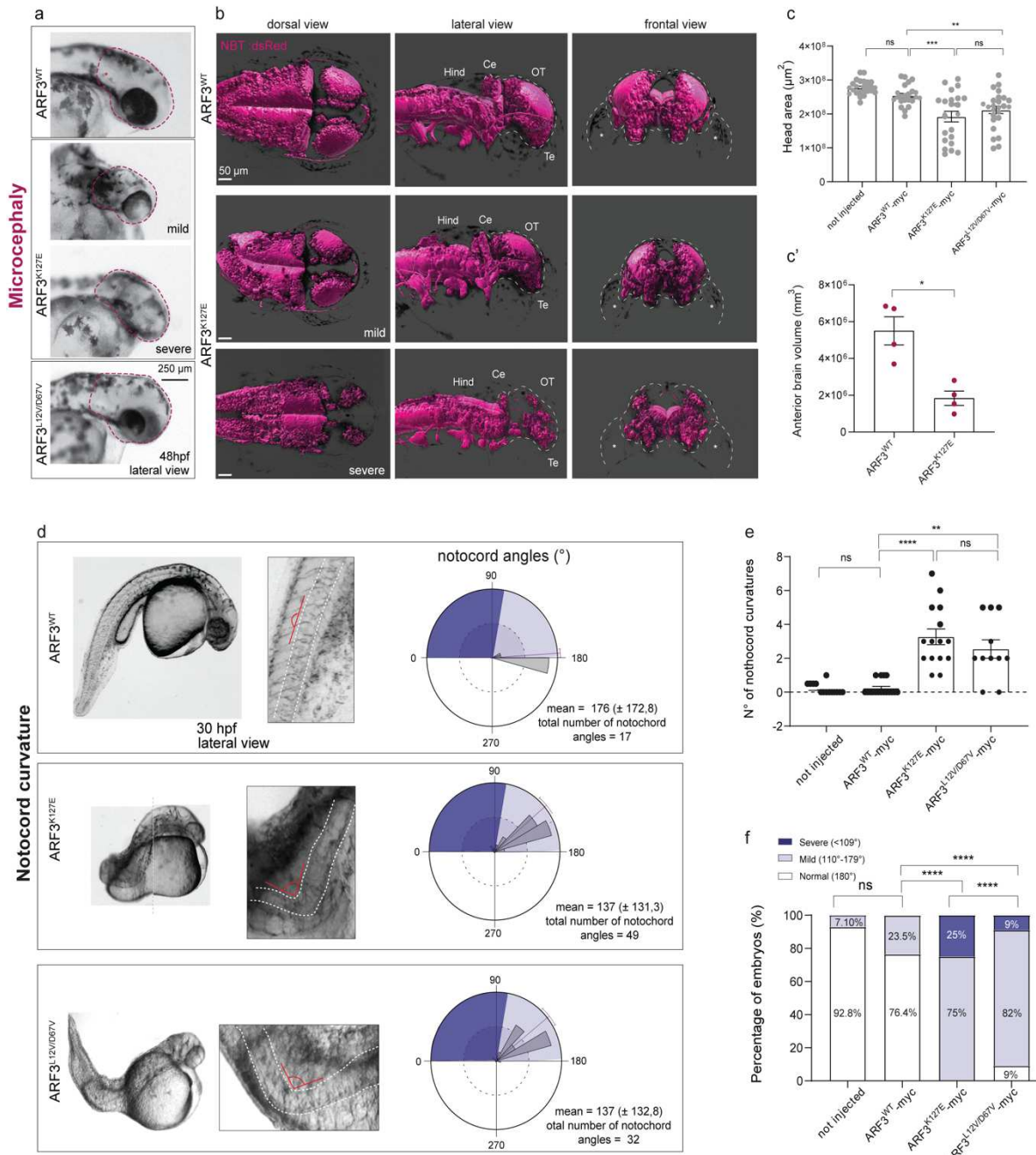
876 **Figure 2. Expression, stability and GTPase activity of WT and mutant ARF3**
877 **protein in COS-1 cells.** (a) Expression levels of each mutant myc-tagged ARF3
878 protein assessed in transiently transfected COS-1 cells via immunoblot. (b) Western
879 blot analysis shows the protein levels of WT ARF3 and ARF3^{K127E} and ARF3^{L12V/D67V}
880 mutants in transfected COS-1 cells, basally and after treatment with MG132 (100 µM)

and baflomycin A1 (200 nM) for six hours. **(c)** Pull-down assay using GGA3-conjugated beads shows ARF3 activation in COS-1 cells transiently expressing WT or mutant myc-tagged ARF3 proteins. Active and total ARF3 levels are monitored using anti-myc antibody. Representative blots and mean ± standard error (SEM) of three independent experiments are shown. Statistical differences are obtained by one-way Anova **(a,c)** followed by Dunnet post hoc test and two-way Anova **(b)** (ns = not significant, * p < 0.05, **p < 0.01, ***p < 0.001, **** p < 0.0001). For the ARF3^{L12V;D67V} mutant the statistical comparison between no treatment (-) and treatment with MG132 results in p=0.07 indicating an overall trend towards increased expression levels of the mutant ARF3 following the treatment.

Dominantly acting variants in ARF3 have disruptive consequences on Golgi integrity and cause microcephaly recapitulated in zebrafish
 Fasano, Muto, Radio, et al.



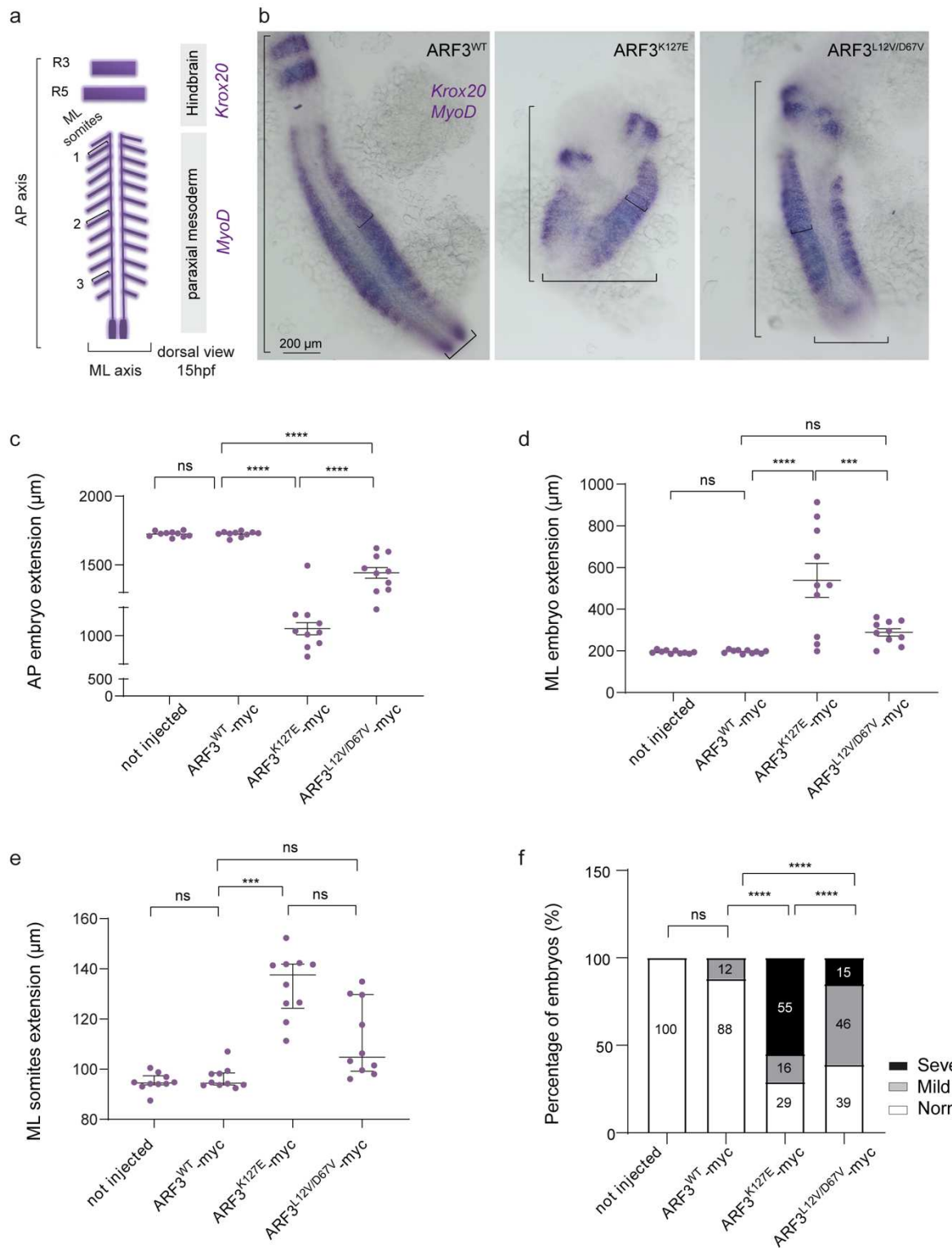
892 **Figure 3. Trans-Golgi fragmentation in cells and zebrafish embryos expressing**
893 **the mutant mCherry-tagged ARF3^{K127E}.** (a) Schematic representation of the
894 experimental set up in both *in vitro* and *in vivo* systems. COS-1 cells are transfected
895 with DNA constructs expressing WT and mutant ARF3-mCherry (magenta) and EGFP-
896 GalT (*trans*-Golgi marker, green) and analyzed by live confocal microscopy between 4-
897 6 hours post transfection. Zebrafish embryos are injected at 1 cell stage with WT and
898 mutant ARF3-mCherry and EGFP-GalT mRNA. mKOFP CAAX mRNA is used as
899 membrane marker (cyan). Animals are analyzed by live confocal microscopy during
900 gastrulation (~6-7 hpf). (b, c) Maximum intensity projections of representative confocal
901 images from a time-lapse experiment ([Video S1](#)) performed in transfected COS-1 cells
902 at 15 min (~4 hours post transfection) and 120 min later (~6 hours post transfection)
903 from the start of the time-lapse experiment. The images show diffused EGFP-GalT
904 signal (*trans*-Golgi fragmentation) in ARF3^{K127E} over time (white arrows). Scale bar =
905 20μm. (d,e) Representative 3D image reconstructions from live confocal z-stack
906 acquisitions of the animal pole in developing zebrafish embryos expressing ARF3^{WT}
907 and ARF3^{K127E} at the mid-gastrulation stage (between 6-7 hpf). White arrowheads
908 indicate a compact *trans*-Golgi morphology surrounding the nucleus (“ribbon”) in the
909 envelope layer cells. Yellow arrowheads indicate cells showing “*punta*” morphology of
910 the TG dispersed throughout the cytosol. Scale bar = 500μm.



911

912 **Figure 4. Zebrafish embryos expressing ARF3 mutant proteins show**
 913 **microcephaly and axial defects with notochord curvatures of variable severities.**
 914 (a) Representative bright field images of the head (purple dashed line) in fish injected
 915 with ARF3 WT or ARF3 K^{127E} and ARF3 $L^{12VD67V}$ mutants at 48 hpf, scale bar = 250 μ m.
 916 (b) Volumetric reconstructions from live confocal acquisitions of whole brains in 48 hpf
 917 *Tg(NBT:dsRed)* fish injected with ARF3 WT and ARF3 K^{127E} show examples of mild and

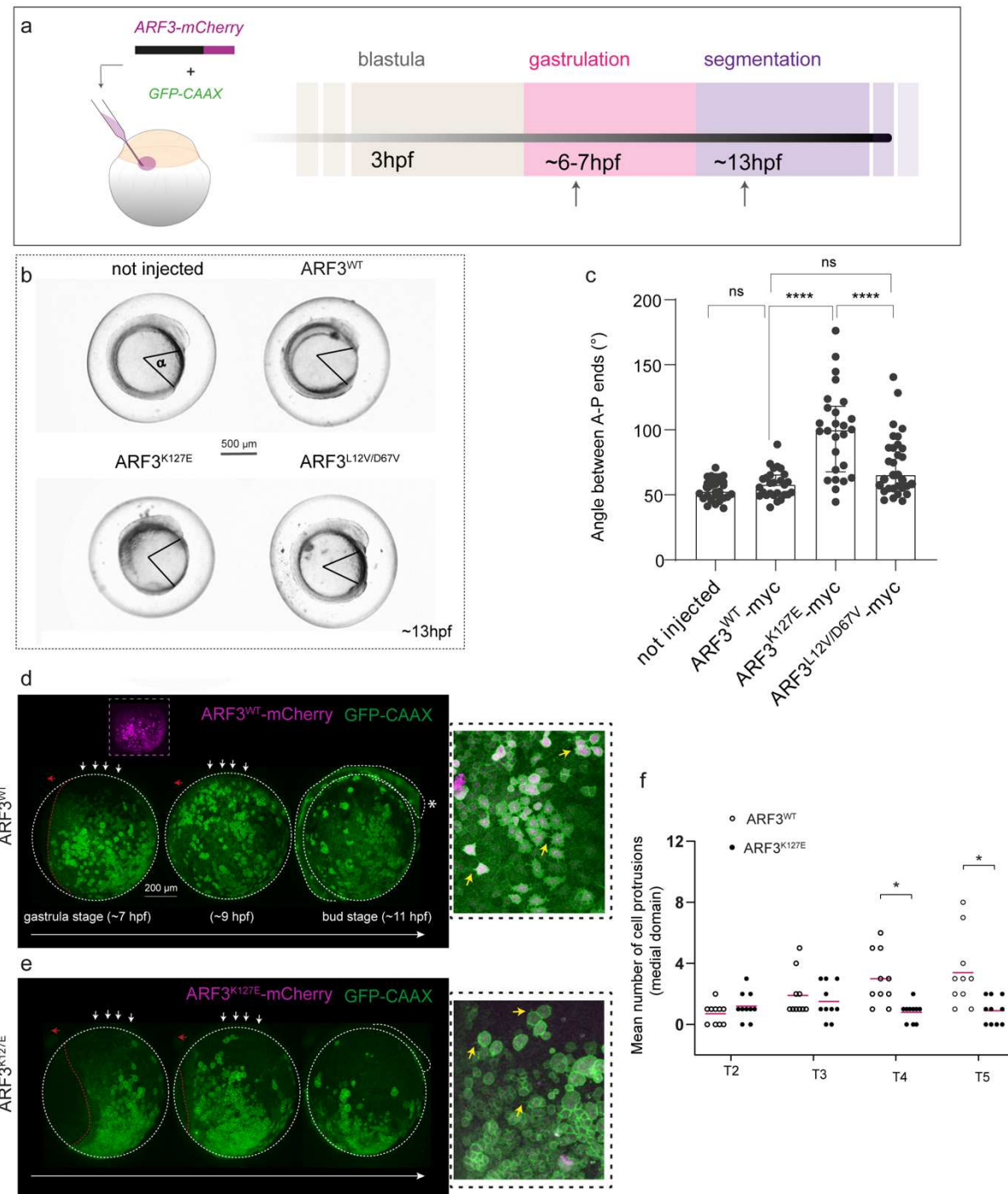
918 severe microcephaly, scale bar = 50 μ m. Te: telencephalon, OT: optic tectum, ce:
919 cerebellum, hind: hindbrain. **(c)** Head area (indicated by the purple dashed contour in
920 a) in ARF3^{K127E} (n = 22) and ARF3^{L12V;D67V} (n = 25) not injected controls (n = 25) and
921 ARF3^{WT} (n = 26) expressing fish. **(c')** Brain volume in *Tg(NBT:dsRed)* fish at 48hpf, n
922 =4. **(d)** Representative bright field images of notochord curvatures (red angle
923 calculated on single notochords), classified as normal (angle = 180°), mild (179°
924 >angle>110°) and severe (109°>angle>0°), in fish expressing ARF3^{WT}, ARF3^{K127E} and
925 ARF3^{L12V;D67V} at 30 hpf. The rose diagrams show the distributions of angles for each
926 set of notochordal observations. **(e)** Number of notochord curvatures in embryos
927 expressing mutant or WT ARF3. **(f)** Incidence of embryos showing notochord
928 curvatures. In e and f n = 14, 17, 15, 11 for not injected, ARF3^{WT}, ARF3^{K127E} and
929 ARF3^{L12V;D67V}, respectively. Data are plotted as mean \pm SEM (c,c'), median with
930 interquartile range (e) or percentage of embryos (f) from two (c,c'), or three (e, f)
931 batches of embryos. One-way ANOVA followed by Tukey's *post hoc* test (c), unpaired
932 t-test with Welch's correction (c') non-parametric Kruskal-Wallis test followed by
933 Dunn's *post hoc* test (e) and Fisher's exact test (f) are used to assess statistical
934 significance (ns= not significant, ** p < 0.01, *** p < 0.001, **** p < 0.0001). Multiplicity
935 adjusted P values are reported for (c,c') and (e).



936

937 **Figure 5. Zebrafish embryos expressing ARF3 mutant proteins exhibit defective**
938 **axes formation during segmentation.** (a) Schematic representation of *Krox20* and

939 *MyoD* mRNA localization (light violet), labeling rhombomeres 3 and 5 (hindbrain) and
940 developing somites (in the paraxial mesoderm), respectively, at 15 hpf. Whole-mount
941 *in situ* hybridization is used to measure AP and ML embryo extension and ML
942 extension of somites (1, 2, 3 indicate the anterior, medial and posterior somites,
943 respectively). **(b)** Representative bright field images showing *Krox20* and *MyoD* *in situ*
944 mRNA staining in fish expressing WT and mutant ARF3, aberrant AP and ML axes and
945 somite width are indicated by black square brackets, scale bar = 200 μ m. **(c-e)** AP
946 embryo extension is reduced (c) while ML embryo (d) and somite (e) extension are
947 increased in fish expressing ARF3 mutants, n = 10. **(f)** Frequency of AP and ML
948 extension defects, n = 44, 48, 37 and 33 for not injected, ARF3^{WT}, ARF3^{K127E} and
949 ARF3^{L12V;D67V}, respectively. Unaffected embryos were characterized by an unaltered
950 *MyoD* and *Krox20* mRNA expression compared to not-injected controls, while the
951 mildly and severely affected embryos showed a reduced expression of the two markers
952 along the AP axis and expansion of the ML axis. Severe cases also showed
953 pronounced ML convergence defects, which were evident by the widely separated left
954 and right *MyoD*-positive domains. Data are plotted as mean + SEM (c, d), median with
955 interquartile range (e) or percentage of the embryos (f) from two (c-e) and three (f)
956 batches of embryos. One-way Anova with Tukey's *post hoc* test (c, d), non-parametric
957 Kruskal-Wallis with Dunn's *post hoc* test (e) or Fisher's exact test in a 2×2 contingency
958 table (f; severe vs. normal) (ns= not significant, * p < 0.05, *** p < 0.001, **** p < 0.0001)
959 are used to assess statistical significance. For c, d and e the multiplicity adjusted P
960 values are reported.



961

962 **Figure 6. Overexpression of activating ARF3^{K127E} in zebrafish embryos impairs**
 963 **convergence and extension movements during gastrulation. (a)** Schematics of the
 964 experimental design. mCherry-tagged ARF3 and GFP-tagged CAAX are injected in
 965 one-cell stage embryos and morphometric measurements are performed between 6

966 hpf (gastrulation) and 13 hpf (segmentation). **(b)** Representative bright field images
967 from live embryos injected with ARF3^{WT} and ARF3 mutant mRNAs (K127E and
968 L12V;D67V) at 13 hpf. Lateral view with anterior region on the top is shown. The angle
969 (alpha, black) between the anterior end and posterior end *anlage*, reflecting the extent
970 of antero-posterior (AP) axis extension, is shown. **(c)** Values of the angle alpha
971 showing the extension of the AP axis and measured in ARF3^{WT} and ARF3^{K127E} and
972 ARF3^{L12V;D67V} embryos are shown, with a significant increase recorded in ARF3^{K127E}
973 mutants, n = 30, 29, 26, 31 for not injected, ARF3^{WT}, ARF3^{K127E} and ARF3^{L12V;D67V},
974 respectively. **(d-e)** Confocal images (maximum z-projections) from a live time-lapse
975 experiment showing lateral view of the embryos at different time points during
976 gastrulation. Images show cells labelled with GFP-tagged CAAX protein expression
977 labeling cellular outlines. Expression of mCherry-tagged ARF3^{WT} in the injected
978 embryos is shown in the upper inset. Higher magnifications on the right (black dashed
979 boxes) show cell protrusions (some are indicated with yellow arrows) of medial cells at
980 circa 8 hpf in ARF3^{WT} and ARF3^{K127E} embryos. **(f)** Number of cell protrusions counted
981 for 10 cells located in the medial portion (centre) of the embryo (between 7 and 8 hpf),
982 n = 1. Data are plotted as median with interquartile range from two batches of embryos
983 (c) and mean value of the cells (f). Nonparametric Kruskal-Wallis with Dunn's *post hoc*
984 test (c) or Two-way Anova, with mixed-effects model analysis and Sidak's *post hoc* test
985 (f) (* p < 0.05, ** p < 0.01; **** p < 0.0001) are used to assess statistical significance.
986 For c the multiplicity adjusted P values are reported

References

1. D'Souza-Schorey, C. & Chavrier, P. ARF proteins: roles in membrane traffic and beyond. *Nat. Rev. Mol. Cell Biol.* **7**, 347–358 (2006).
2. Cockcroft, S. *et al.* Phospholipase D: a downstream effector of ARF in granulocytes. *Science* **263**, 523–526 (1994).
3. Guo, Y., Sirkis, D. W. & Schekman, R. Protein Sorting at the trans-Golgi Network. *Annu. Rev. Cell Dev. Biol.* **30**, 169–206 (2014).
4. Makhoul, C., Gosavi, P. & Gleeson, P. A. Golgi Dynamics: The Morphology of the Mammalian Golgi Apparatus in Health and Disease. *Front. Cell Dev. Biol.* **7**, 112 (2019).
5. Wei, J.-H. & Seemann, J. Golgi ribbon disassembly during mitosis, differentiation and disease progression. *Curr. Opin. Cell Biol.* **47**, 43–51 (2017).
6. Seifert, W. *et al.* Cohen syndrome-associated protein, COH1, is a novel, giant Golgi matrix protein required for Golgi integrity. *J. Biol. Chem.* **286**, 37665–37675 (2011).
7. Shamseldin, H. E., Bennett, A. H., Alfadhel, M., Gupta, V. & Alkuraya, F. S. GOLGA2, encoding a master regulator of golgi apparatus, is mutated in a patient with a neuromuscular disorder. *Hum. Genet.* **135**, 245–251 (2016).
8. Rasika, S., Passemard, S., Verloes, A., Gressens, P. & El Ghouzzi, V. Golgipathies in Neurodevelopment: A New View of Old Defects. *Dev. Neurosci.* **40**, 396–416 (2018).
9. Dupuis, N. *et al.* Dymeclin deficiency causes postnatal microcephaly, hypomyelination and reticulum-to-Golgi trafficking defects in mice and humans. *Hum. Mol. Genet.* **24**, 2771–2783 (2015).

Dominantly acting variants in ARF3 have disruptive consequences on Golgi integrity and cause microcephaly recapitulated in zebrafish
Fasano, Muto, Radio, et al.

10. Chavrier, P. & Goud, B. The role of ARF and Rab GTPases in membrane transport. *Curr. Opin. Cell Biol.* **11**, 466–475 (1999).
11. Volpicelli-Daley, L. A., Li, Y., Zhang, C.-J. & Kahn, R. A. Isoform-selective Effects of the Depletion of ADP-Ribosylation Factors 1–5 on Membrane Traffic. *Mol. Biol. Cell* **16**, 4495–4508 (2005).
12. Donaldson, J. G. & Jackson, C. L. ARF family G proteins and their regulators: roles in membrane transport, development and disease. *Nat. Rev. Mol. Cell Biol.* **12**, 362–375 (2011).
13. Zhang, C. J. *et al.* Expression of a dominant allele of human ARF1 inhibits membrane traffic in vivo. *J. Cell Biol.* **124**, 289–300 (1994).
14. Gillingham, A. K. & Munro, S. The small G proteins of the Arf family and their regulators. *Annu. Rev. Cell Dev. Biol.* **23**, 579–611 (2007).
15. Amor, J. C., Harrison, D. H., Kahn, R. A. & Ringe, D. Structure of the human ADP-ribosylation factor 1 complexed with GDP. *Nature* **372**, 704–708 (1994).
16. Kjeldgaard, M., Nyborg, J. & Clark, B. F. The GTP binding motif: variations on a theme. *FASEB J. Off. Publ. Fed. Am. Soc. Exp. Biol.* **10**, 1347–1368 (1996).
17. Goldberg, J. Structural basis for activation of ARF GTPase: mechanisms of guanine nucleotide exchange and GTP-myristoyl switching. *Cell* **95**, 237–248 (1998).
18. Donaldson, J. G., Finazzi, D. & Klausner, R. D. Brefeldin A inhibits Golgi membrane-catalysed exchange of guanine nucleotide onto ARF protein. *Nature* **360**, 350–352 (1992).
19. Helms, J. B. & Rothman, J. E. Inhibition by brefeldin A of a Golgi membrane enzyme that catalyses exchange of guanine nucleotide bound to ARF. *Nature* **360**, 352–354 (1992).

20. Randazzo, P. A., Yang, Y. C., Rulka, C. & Kahn, R. A. Activation of ADP-ribosylation factor by Golgi membranes. Evidence for a brefeldin A- and protease-sensitive activating factor on Golgi membranes. *J. Biol. Chem.* **268**, 9555–9563 (1993).
21. Antonny, B., Huber, I., Paris, S., Chabre, M. & Cassel, D. Activation of ADP-ribosylation factor 1 GTPase-activating protein by phosphatidylcholine-derived diacylglycerols. *J. Biol. Chem.* **272**, 30848–30851 (1997).
22. Randazzo, P. A. Resolution of two ADP-ribosylation factor 1 GTPase-activating proteins from rat liver. *Biochem. J.* **324 (Pt 2)**, 413–419 (1997).
23. Reinhard, C., Schweikert, M., Wieland, F. T. & Nickel, W. Functional reconstitution of COPI coat assembly and disassembly using chemically defined components. *Proc. Natl. Acad. Sci. U. S. A.* **100**, 8253–8257 (2003).
24. Gilbert, C. E., Sztul, E. & Machamer, C. E. Commonly used trafficking blocks disrupt ARF1 activation and the localization and function of specific Golgi proteins. *Mol. Biol. Cell* **29**, 937–947 (2018).
25. Munro, S. The golgin coiled-coil proteins of the Golgi apparatus. *Cold Spring Harb. Perspect. Biol.* **3**, a005256 (2011).
26. Kulkarni-Gosavi, P., Makhoul, C. & Gleeson, P. A. Form and function of the Golgi apparatus: scaffolds, cytoskeleton and signalling. *FEBS Lett.* **593**, 2289–2305 (2019).
27. Kondo, Y. et al. ARF1 and ARF3 are required for the integrity of recycling endosomes and the recycling pathway. *Cell Struct. Funct.* **37**, 141–154 (2012).
28. Dascher, C. & Balch, W. E. Dominant inhibitory mutants of ARF1 block endoplasmic reticulum to Golgi transport and trigger disassembly of the Golgi apparatus. *J. Biol. Chem.* **269**, 1437–1448 (1994).

29. Altan-Bonnet, N., Phair, R. D., Polishchuk, R. S., Weigert, R. & Lippincott-Schwartz, J. A role for Arf1 in mitotic Golgi disassembly, chromosome segregation, and cytokinesis. *Proc. Natl. Acad. Sci. U. S. A.* **100**, 13314–13319 (2003).
30. Hanai, A. *et al.* Class I Arfs (Arf1 and Arf3) and Arf6 are localized to the Flemming body and play important roles in cytokinesis. *J. Biochem. (Tokyo)* **159**, 201–208 (2016).
31. Nakayama, K. Regulation of cytokinesis by membrane trafficking involving small GTPases and the ESCRT machinery. *Crit. Rev. Biochem. Mol. Biol.* **51**, 1–6 (2016).
32. Rodrigues, F. F. & Harris, T. J. C. Key roles of Arf small G proteins and biosynthetic trafficking for animal development. *Small GTPases* **10**, 403–410 (2019).
33. Carvajal-Gonzalez, J. M. *et al.* The clathrin adaptor AP-1 complex and Arf1 regulate planar cell polarity in vivo. *Nat. Commun.* **6**, 6751 (2015).
34. Ge, X. *et al.* Missense-depleted regions in population exomes implicate ras superfamily nucleotide-binding protein alteration in patients with brain malformation. *NPJ Genomic Med.* **1**, (2016).
35. Sobreira, N., Schiettecatte, F., Valle, D. & Hamosh, A. GeneMatcher: a matching tool for connecting investigators with an interest in the same gene. *Hum. Mutat.* **36**, 928–930 (2015).
36. Denayer, E. *et al.* Mutation analysis in Costello syndrome: functional and structural characterization of the HRAS p.Lys117Arg mutation. *Hum. Mutat.* **29**, 232–239 (2008).
37. Lim, Y. H. *et al.* Somatic Activating RAS Mutations Cause Vascular Tumors Including Pyogenic Granuloma. *J. Invest. Dermatol.* **135**, 1698–1700 (2015).
38. Schubbert, S. *et al.* Germline KRAS mutations cause Noonan syndrome. *Nat. Genet.* **38**, 331–336 (2006).

Dominantly acting variants in ARF3 have disruptive consequences on Golgi integrity and cause microcephaly recapitulated in zebrafish
Fasano, Muto, Radio, et al.

39. Zenker, M. *et al.* Expansion of the genotypic and phenotypic spectrum in patients with KRAS germline mutations. *J. Med. Genet.* **44**, 131–135 (2007).
40. Landrum, M. J. *et al.* ClinVar: improving access to variant interpretations and supporting evidence. *Nucleic Acids Res.* **46**, D1062–D1067 (2018).
41. Nava, C. *et al.* Cardio-facio-cutaneous and Noonan syndromes due to mutations in the RAS/MAPK signalling pathway: genotype-phenotype relationships and overlap with Costello syndrome. *J. Med. Genet.* **44**, 763–771 (2007).
42. Gripp, K. W. & Lin, A. E. Costello syndrome: a Ras/mitogen activated protein kinase pathway syndrome (rasopathy) resulting from HRAS germline mutations. *Genet. Med. Off. J. Am. Coll. Med. Genet.* **14**, 285–292 (2012).
43. Lee, Y. *et al.* Makes caterpillars floppy-like effector-containing MARTX toxins require host ADP-ribosylation factor (ARF) proteins for systemic pathogenicity. *Proc. Natl. Acad. Sci. U. S. A.* **116**, 18031–18040 (2019).
44. Carta, C. *et al.* Germline missense mutations affecting KRAS Isoform B are associated with a severe Noonan syndrome phenotype. *Am. J. Hum. Genet.* **79**, 129–135 (2006).
45. Zampino, G. *et al.* Diversity, parental germline origin, and phenotypic spectrum of de novo HRAS missense changes in Costello syndrome. *Hum. Mutat.* **28**, 265–272 (2007).
46. Pasqualato, S., Renault, L. & Chéfils, J. Arf, Arl, Arp and Sar proteins: a family of GTP-binding proteins with a structural device for ‘front-back’ communication. *EMBO Rep.* **3**, 1035–1041 (2002).
47. Ménétrey, J. *et al.* Structural basis for ARF1-mediated recruitment of ARHGAP21 to Golgi membranes. *EMBO J.* **26**, 1953–1962 (2007).

Dominantly acting variants in ARF3 have disruptive consequences on Golgi integrity and cause microcephaly recapitulated in zebrafish
Fasano, Muto, Radio, et al.

48. Yu, X., Breitman, M. & Goldberg, J. A Structure-Based Mechanism for Arf1-Dependent Recruitment of Coatomer to Membranes. *Cell* **148**, 530–542 (2012).
49. Ratcliffe, C. D. H., Sahgal, P., Parachoniak, C. A., Ivaska, J. & Park, M. Regulation of Cell Migration and $\beta 1$ Integrin Trafficking by the Endosomal Adaptor GGA3. *Traffic Cph. Den.* **17**, 670–688 (2016).
50. Adolf, F. et al. Proteomic Profiling of Mammalian COPII and COPI Vesicles. *Cell Rep.* **26**, 250–265.e5 (2019).
51. Xiang, Y., Seemann, J., Bisel, B., Punthambaker, S. & Wang, Y. Active ADP-ribosylation factor-1 (ARF1) is required for mitotic Golgi fragmentation. *J. Biol. Chem.* **282**, 21829–21837 (2007).
52. Manolea, F. et al. Arf3 is activated uniquely at the trans-Golgi network by brefeldin A-inhibited guanine nucleotide exchange factors. *Mol. Biol. Cell* **21**, 1836–1849 (2010).
53. Kimmel, C. B., Ballard, W. W., Kimmel, S. R., Ullmann, B. & Schilling, T. F. Stages of embryonic development of the zebrafish. *Dev. Dyn. Off. Publ. Am. Assoc. Anat.* **203**, 253–310 (1995).
54. Bagwell, J. et al. Notochord vacuoles absorb compressive bone growth during zebrafish spine formation. *eLife* **9**, (2020).
55. Jessen, J. R. et al. Zebrafish trilobite identifies new roles for Strabismus in gastrulation and neuronal movements. *Nat. Cell Biol.* **4**, 610–615 (2002).
56. Roszko, I., Sawada, A. & Solnica-Krezel, L. Regulation of convergence and extension movements during vertebrate gastrulation by the Wnt/PCP pathway. *Semin. Cell Dev. Biol.* **20**, 986–997 (2009).
57. Wallingford, J. B., Fraser, S. E. & Harland, R. M. Convergent extension: the molecular control of polarized cell movement during embryonic development. *Dev. Cell* **2**, 695–706 (2002).

Dominantly acting variants in ARF3 have disruptive consequences on Golgi integrity and cause microcephaly recapitulated in zebrafish
Fasano, Muto, Radio, et al.

58. Tate, J. G. *et al.* COSMIC: the Catalogue Of Somatic Mutations In Cancer. *Nucleic Acids Res.* **47**, D941–D947 (2019).
59. Tartaglia, M. & Gelb, B. D. Disorders of dysregulated signal traffic through the RAS-MAPK pathway: phenotypic spectrum and molecular mechanisms. *Ann. N. Y. Acad. Sci.* **1214**, 99–121 (2010).
60. Motta, M. *et al.* Activating MRAS mutations cause Noonan syndrome associated with hypertrophic cardiomyopathy. *Hum. Mol. Genet.* **29**, 1772–1783 (2020).
61. Flex, E. *et al.* Activating mutations in RRAS underlie a phenotype within the RASopathy spectrum and contribute to leukaemogenesis. *Hum. Mol. Genet.* **23**, 4315–4327 (2014).
62. Niihori, T. *et al.* Germline-Activating RRAS2 Mutations Cause Noonan Syndrome. *Am. J. Hum. Genet.* **104**, 1233–1240 (2019).
63. Capri, Y. *et al.* Activating Mutations of RRAS2 Are a Rare Cause of Noonan Syndrome. *Am. J. Hum. Genet.* **104**, 1223–1232 (2019).
64. Khan, A. R. & Ménétrey, J. Structural biology of Arf and Rab GTPases' effector recruitment and specificity. *Struct. Lond. Engl. 1993* **21**, 1284–1297 (2013).
65. Merithew, E. *et al.* Structural Plasticity of an Invariant Hydrophobic Triad in the Switch Regions of Rab GTPases Is a Determinant of Effector Recognition*. *J. Biol. Chem.* **276**, 13982–13988 (2001).
66. Kuai, J. & Kahn, R. A. Residues forming a hydrophobic pocket in ARF3 are determinants of GDP dissociation and effector interactions. *FEBS Lett.* **487**, 252–256 (2000).
67. Banne, E. *et al.* West syndrome, microcephaly, grey matter heterotopia and hypoplasia of corpus callosum due to a novel ARFGEF2 mutation. *J. Med. Genet.* **50**, 772–775 (2013).

Dominantly acting variants in ARF3 have disruptive consequences on Golgi integrity and cause microcephaly recapitulated in zebrafish
Fasano, Muto, Radio, et al.

68. Horton, A. C. *et al.* Polarized Secretory Trafficking Directs Cargo for Asymmetric Dendrite Growth and Morphogenesis. *Neuron* **48**, 757–771 (2005).
69. Lauri, A., Fasano, G., Venditti, M., Dallapiccola, B. & Tartaglia, M. In vivo functional genomics for undiagnosed patients: the impact of small GTPases signaling dysregulation at pan-embryo developmental scale. *Front. Cell Dev. Biol.* **9**, (2021).
70. Prigozhina, N. L. & Waterman-Storer, C. M. Decreased polarity and increased random motility in PtK1 epithelial cells correlate with inhibition of endosomal recycling. *J. Cell Sci.* **119**, 3571–3582 (2006).
71. Winter, J. F. *et al.* *Caenorhabditis elegans* screen reveals role of PAR-5 in RAB-11-recycling endosome positioning and apicobasal cell polarity. *Nat. Cell Biol.* **14**, 666–676 (2012).
72. Ulrich, F. *et al.* Wnt11 Functions in Gastrulation by Controlling Cell Cohesion through Rab5c and E-Cadherin. *Dev. Cell* **9**, 555–564 (2005).
73. Sarmah, S. *et al.* Sec24D-dependent transport of extracellular matrix proteins is required for zebrafish skeletal morphogenesis. *PLoS One* **5**, e10367 (2010).
74. Coutinho, P. *et al.* Differential requirements for COPI transport during vertebrate early development. *Dev. Cell* **7**, 547–558 (2004).
75. Sheen, V. L. *et al.* Mutations in ARFGEF2 implicate vesicle trafficking in neural progenitor proliferation and migration in the human cerebral cortex. *Nat. Genet.* **36**, 69–76 (2004).
76. Pezzani, L. *et al.* Atypical presentation of pediatric BRAF RASopathy with acute encephalopathy. *Am. J. Med. Genet. A.* **176**, 2867–2871 (2018).
77. Ziegler, A. *et al.* Confirmation that variants in TTI2 are responsible for autosomal recessive intellectual disability. *Clin. Genet.* **96**, 354–358 (2019).

Dominantly acting variants in ARF3 have disruptive consequences on Golgi integrity and cause microcephaly recapitulated in zebrafish
Fasano, Muto, Radio, et al.

78. Radio, F. C. *et al.* SPEN haploinsufficiency causes a neurodevelopmental disorder overlapping proximal 1p36 deletion syndrome with an episignature of X chromosomes in females. *Am. J. Hum. Genet.* **108**, 502–516 (2021).
79. Lin, Y.-C. *et al.* SCUBE3 loss-of-function causes a recognizable recessive developmental disorder due to defective bone morphogenetic protein signaling. *Am. J. Hum. Genet.* **108**, 115–133 (2021).
80. Vetro, A. *et al.* ATP1A2- and ATP1A3-associated early profound epileptic encephalopathy and polymicrogyria. *Brain J. Neurol.* (2021)
doi:10.1093/brain/awab052.
81. Humphrey, W., Dalke, A. & Schulten, K. VMD: visual molecular dynamics. *J. Mol. Graph.* **14**, 33–38, 27–28 (1996).
82. Waterhouse, A. *et al.* SWISS-MODEL: homology modelling of protein structures and complexes. *Nucleic Acids Res.* **46**, W296–W303 (2018).
83. Pettersen, E. F. *et al.* UCSF Chimera--a visualization system for exploratory research and analysis. *J. Comput. Chem.* **25**, 1605–1612 (2004).
84. Dunbrack, R. L. Rotamer libraries in the 21st century. *Curr. Opin. Struct. Biol.* **12**, 431–440 (2002).
85. Páll, S. *et al.* Heterogeneous parallelization and acceleration of molecular dynamics simulations in GROMACS. *J. Chem. Phys.* **153**, 134110 (2020).
86. Huang, J. & MacKerell, A. D. CHARMM36 all-atom additive protein force field: validation based on comparison to NMR data. *J. Comput. Chem.* **34**, 2135–2145 (2013).
87. Bussi, G., Donadio, D. & Parrinello, M. Canonical sampling through velocity rescaling. *J. Chem. Phys.* **126**, 014101 (2007).

Dominantly acting variants in ARF3 have disruptive consequences on Golgi integrity and cause microcephaly recapitulated in zebrafish
Fasano, Muto, Radio, et al.

88. Darden, T., York, D. & Pedersen, L. Particle mesh Ewald: An N·log(N) method for Ewald sums in large systems. *J. Chem. Phys.* **98**, 10089–10092 (1993).
89. Villefranc, J. A., Amigo, J. & Lawson, N. D. Gateway compatible vectors for analysis of gene function in the zebrafish. *Dev. Dyn. Off. Publ. Am. Assoc. Anat.* **236**, 3077–3087 (2007).
90. Don, E. K. *et al.* A Tol2 Gateway-Compatible Toolbox for the Study of the Nervous System and Neurodegenerative Disease. *Zebrafish* **14**, 69–72 (2017).
91. Cole, N. B. *et al.* Diffusional mobility of Golgi proteins in membranes of living cells. *Science* **273**, 797–801 (1996).
92. Makyio, H. *et al.* Structural basis for Arf6-MKLP1 complex formation on the Flemming body responsible for cytokinesis. *EMBO J.* **31**, 2590–2603 (2012).
93. LaFave, M. C., Varshney, G. K., Vemulapalli, M., Mullikin, J. C. & Burgess, S. M. A defined zebrafish line for high-throughput genetics and genomics: NHGRI-1. *Genetics* **198**, 167–170 (2014).
94. Peri, F. & Nüsslein-Volhard, C. Live Imaging of Neuronal Degradation by Microglia Reveals a Role for v0-ATPase a1 in Phagosomal Fusion In Vivo. *Cell* **133**, 916–927 (2008).
95. Westerfield, M. *The zebrafish book. A guide for the laboratory use of zebrafish (Danio rerio)*. (2000).
96. Kovach, W. L. *Oriana – Circular Statistics for Windows*. (2011).
97. Thisse, C. & Thisse, B. High-resolution *in situ* hybridization to whole-mount zebrafish embryos. *Nat. Protoc.* **3**, 59–69 (2008).
98. Schindelin, J. *et al.* Fiji: an open-source platform for biological-image analysis. *Nat. Methods* **9**, 676–682 (2012).

Supplementary Files

This is a list of supplementary files associated with this preprint. Click to download.

- [FasanoMutoRadioTable1.pdf](#)
- [SupplementaryInformationFasanoMutoRadioetal20210107021.pdf](#)
- [SupplementaryVideo1.mp4](#)